



# A Long Stream of Metal-poor Cool Gas around a Massive Starburst Galaxy at $z = 2.67$

Hai Fu<sup>1,2</sup>, R. Xue<sup>1,3</sup>, J. X. Prochaska<sup>4</sup>, A. Stockton<sup>2</sup>, S. Ponnada<sup>1,5</sup>, M. W. Lau<sup>6</sup>, A. Cooray<sup>7</sup>, and D. Narayanan<sup>8</sup><sup>1</sup>Department of Physics & Astronomy, University of Iowa, Iowa City, IA 52242, USA; [hai-fu@uiowa.edu](mailto:hai-fu@uiowa.edu)<sup>2</sup>Institute for Astronomy, University of Hawaii, Honolulu, HI 96822, USA<sup>3</sup>National Radio Astronomy Observatory, Charlottesville, VA, 22903, USA<sup>4</sup>Department of Astronomy and Astrophysics, UCO/Lick Observatory, University of California, Santa Cruz, CA 95064, USA<sup>5</sup>Astronomy Department, California Institute of Technology, Pasadena, CA 91125, USA<sup>6</sup>Department of Physics and Astronomy, University of California, Riverside, CA 92521, USA<sup>7</sup>Department of Physics and Astronomy, University of California, Irvine, CA 92697, USA<sup>8</sup>Department of Astronomy, University of Florida, Gainesville, FL 32611, USA

Received 2020 December 23; revised 2021 January 7; accepted 2021 January 11; published 2021 February 24

## Abstract

We present the first detailed dissection of the circumgalactic medium (CGM) of massive starburst galaxies at  $z > 2$ . Our target is a submillimeter galaxy (SMG) at  $z = 2.674$  that has a star formation rate of  $1200 M_{\odot} \text{ yr}^{-1}$  and a molecular gas reservoir of  $1.3 \times 10^{11} M_{\odot}$ . We characterize its CGM with two background QSOs at impact parameters of 93 kpc and 176 kpc. We detect strong HI and metal-line absorption near the redshift of the SMG toward both QSOs, each consisting of three main subsystems spanning over  $1500 \text{ km s}^{-1}$ . The absorbers show remarkable kinematic and metallicity coherence across a separation of  $\sim 86$  kpc. In particular, the cool gas in the CGM of the SMG exhibits high HI column densities ( $\log(N_{\text{HI}}/\text{cm}^{-2}) = 20.2, 18.6$ ), a low metallicity ( $[M/H] \approx -2.0$ ), and nearly the same radial velocity ( $\delta v \sim -300 \text{ km s}^{-1}$ ). While the HI column densities match previous results on the massive halos hosting QSOs, the metallicity is lower by more than an order of magnitude, making it an outlier in the line width–metallicity relation of damped Ly $\alpha$  absorbers. The large physical extent, the velocity coherence, the high surface densities, and the low metallicity are all consistent with the cool, inflowing, and near-pristine gas streams predicted to penetrate hot massive halos at  $z > 1.5$ . We estimate a total gas accretion rate of  $\sim 100 M_{\odot} \text{ yr}^{-1}$  from three such streams. At this rate, it takes only a gigayear to acquire the molecular gas reservoir of the central starburst.

*Unified Astronomy Thesaurus concepts:* Starburst galaxies (1570); Circumgalactic medium (1879)

## 1. Introduction

The global gas supply for in situ star formation is a central question in galaxy formation and evolution, because star formation and merging are the two primary channels through which galaxies grow (Oser et al. 2010). According to spherical hydrodynamical models (Birboim & Dekel 2003) and cosmological simulations (Keres et al. 2005), stable accretion shocks are established near the virial radius when a dark matter (DM) halo grows to a mass threshold of  $M_{\text{shock}} = 2\text{--}3 \times 10^{11} M_{\odot}$ . In massive halos, a significant fraction of the accreted gas is expected to be shock-heated to the virial temperature ( $T_{\text{vir}} = 8 \times 10^6 (M_{\text{halo}}/10^{13} M_{\odot})^{2/3} \text{ K}$ ) and develops an atmosphere of hot diffuse gas. The virial shock effectively cuts off the fuel supply for star formation, because of the inefficient radiative cooling of the hot gas even in the denser inner regions (Kereš et al. 2009). But at high redshift, narrow filaments of cool gas ( $T \lesssim 10^5 \text{ K}$ ) from the cosmic web may penetrate the hot atmospheres of rare, massive halos without ever being shock-heated to the virial temperature, thanks to the lower masses of typical halos at higher redshifts that define the width of the filaments (Dekel & Birboim 2006; Dekel et al. 2009). In fact, this *cold mode* accretion may dominate over the *hot mode* accretion (radiative cooling of shock-heated virialized gas) at all halo masses at  $z > 2$  (Kereš et al. 2009).

In emission, the predicted cold-mode accretion streams (or “cold streams” in short) feeding high-redshift massive galaxies may appear as giant filamentary Ly $\alpha$  nebulae around QSOs (Weidinger et al. 2004; Cantalupo et al. 2014; Martin et al. 2015, 2019) and in dense protocluster environments (Møller & Fynbo 2001; Hennawi et al. 2015; Li et al. 2019; Umehata et al. 2019;

Daddi et al. 2020). However, it has been difficult to rule out outflows as the alternative interpretation, especially when QSO photoionization contributes to the Ly $\alpha$  emission and the chemical abundance of the nebulae cannot be easily measured. In absorption, cold streams can be detected and distinguished from other gaseous components based on neutral hydrogen (HI) column density, kinematics, and particularly chemical abundance (Fumagalli et al. 2011; Theuns 2021).

In this project, we have selected a sample of massive starbursts at high redshifts in the vicinity of background QSOs to trace the cool gas supply in these early massive halos. There, the problem of gas supply is the most acute because of the extremely short gas exhaustion timescale. We then utilize the absorption-line spectra of background QSOs to characterize the physical state of their circumgalactic medium (CGM)—the gas between the inner regions of galaxies and the diffuse intergalactic medium (IGM)—and to search for large-scale cool gas reservoirs. In this section, we review our knowledge of the target galaxy sample and QSO absorption-line systems in the literature. These earlier studies have motivated this project and will provide valuable reference samples that can be compared with the system dissected in this work.

### 1.1. Submillimeter Galaxies

Heated dust in the interstellar medium cools by emitting a modified blackbody spectrum (MBB;  $S_{\nu} \propto (1 - e^{-\tau_{\nu}}) B_{\nu}(T)$ ) with temperatures in the range  $10 \text{ K} \lesssim T \lesssim 100 \text{ K}$ , forming the far-infrared (IR) hump in the spectral energy distribution (SED) of a galaxy. At any given frequency along the Rayleigh–Jeans tail where the dust should be optically thin, the observed flux

density ( $S_{\nu,\text{obs}}$ ) of the MBB is proportional to the dust mass ( $M_{\text{dust}}$ ), the dust temperature ( $T$ ), and the redshift ( $z$ ):

$$\begin{aligned} S_{\nu,\text{obs}} &\propto M_{\text{dust}} T (1+z)^{\beta-1} \nu_{\text{obs}}^{2+\beta} / d_A(z)^2 \\ &\propto M_{\text{dust}} T (1+z)^{\beta-1}, \end{aligned} \quad (1)$$

where  $d_A(z)$  is the angular diameter distance at redshift  $z$  (which varies by only 22% between  $z = 1$  and  $z = 4$ ) and  $\beta \approx 2$  is the dust emissivity parameter ( $\kappa_{\nu} \propto \nu^{\beta}$ ). Therefore, galaxies selected at long wavelengths, such as the (sub)millimeter regime, preferentially have higher dust mass, higher dust temperature, and are at higher redshift than galaxies selected at shorter wavelengths. Furthermore, holding the metallicity ( $Z_{\text{gas}}$ ) constant, high dust mass together with high temperature implies that the galaxies are gas-rich ( $M_{\text{gas}} = M_{\text{dust}}/Z_{\text{gas}}$ ) and have high star formation efficiency ( $\text{SFE} = \text{SFR}/M_{\text{gas}}$ , where SFR is the star formation rate), because

$$T^4 \propto L_{\text{bol}}/M_{\text{dust}} \propto \text{SFR}/(Z_{\text{gas}}M_{\text{gas}}), \quad (2)$$

a result from the Stefan–Boltzmann law.

Indeed, follow-up observations of the brightest galaxies selected at  $850 \mu\text{m}$  ( $S_{850} \gtrsim 3 \text{ mJy}$ ), i.e., the submillimeter galaxies (SMGs; Smail et al. 1997; Barger et al. 1998; Blain et al. 2002), have revealed a significant population of gas-rich starburst galaxies that contribute almost as much to the cosmic SFR density as UV-selected Lyman break galaxies at  $z = 2\text{--}3$  (Chapman et al. 2005; Casey et al. 2014). The SMGs are mature ( $\langle M_{\text{star}} \rangle \sim 10^{11} M_{\odot}$ ; Hainline et al. 2011; Michałowski et al. 2012; Targett et al. 2013), metal-rich ( $\langle Z \rangle \sim Z_{\odot}$ ; Swinbank et al. 2004), gas-rich ( $\langle M_{\text{mol}} \rangle \sim 3 \times 10^{10} M_{\odot}$ ; Greve et al. 2005; Tacconi et al. 2008; Ivison et al. 2011; Bothwell et al. 2013), extreme star-forming systems ( $\overline{\text{SFR}} \sim 500 M_{\odot} \text{ yr}^{-1}$ ) with a broad redshift distribution that peaks at  $\langle z \rangle \sim 2.5$  (Chapman et al. 2005; Wardlow et al. 2011). The molecular gas reservoirs are turbulent, likely due to starburst-driven galactic outflows (Falgarone et al. 2017). Notably, the nearly linear relation between CO and IR luminosities implies an almost constant gas depletion timescale of  $\tau_{\text{dep}} \equiv M_{\text{mol}}/\text{SFR} \sim 0.1 \text{ Gyr}$  (Bothwell et al. 2013), which is far shorter than that of normal star-forming galaxies on the main sequence ( $\tau_{\text{dep}} \sim 0.6 \text{ Gyr}$  at  $z = 2.5$ ; Tacconi et al. 2018), justifying the usage of “starburst” in describing SMGs.<sup>9</sup>

On the other hand, the autocorrelation length for SMGs of  $\sim 11 \text{ Mpc}$  at  $z = 1\text{--}3$  implies a characteristic dark matter halo mass of  $M_{\text{halo}} \sim 9 \times 10^{12} M_{\odot}$  for  $h = 0.7$  (Hickox et al. 2012). The high halo mass is consistent with the high maximum rotation velocities ( $V_{\text{circ}} \gtrsim 500 \text{ km s}^{-1}$ ) observed in several bright SMGs with spatially resolved kinematics (e.g., Hodge et al. 2012; Xue et al. 2018). For Navarro–Frenk–White (NFW) halos (Navarro et al. 1996) at  $z = 2.5$ , the halo mass is directly related to the maximum circular velocity by a power law:  $M_{\text{halo}} = 10^{13} M_{\odot} (V_{\text{circ}}/500 \text{ km s}^{-1})^3$  (Bullock et al. 2001; Klypin et al. 2011). Such a mass is well above the threshold mass for stable virial shocks ( $M_{\text{shock}}$ ), and atmospheres of hot

gas at the virial temperature ( $\sim 8 \times 10^6 \text{ K}$ ) are expected to fill the halo. But as previously discussed, at the early epoch of the SMGs, cool gas filaments can penetrate their halos, which could potentially deliver enough gas to build the molecular gas reservoir that supports the ongoing intense star formation.

## 1.2. QSO Absorption-line Systems

Ever since the discovery of multiple absorption redshifts in QSO spectra (Burbidge et al. 1968), quasar absorption-line spectroscopy has become a powerful tool to study diffuse gas at various phases in the IGM and the CGM, which account for the majority of the baryonic mass in the universe (see Péroux & Howk 2020 for a recent review). The optical depth at the Lyman limit ( $\lambda_{\text{rest}} = 912 \text{ \AA}$ ) reaches unity when the H I column density reaches  $\log N_{\text{H I}} = 17.2$ <sup>10</sup>. Accumulating evidence suggests that these optically thick absorbers trace material in virialized structures (i.e., the CGM, Fumagalli et al. 2016; Lehner et al. 2016), while the optically thin absorbers in the Ly $\alpha$  forest (LYAF) likely trace the IGM (Rauch 1998). Due to their distinct physical properties, the optically thick absorbers are empirically subdivided into three categories based on their H I column densities: the Lyman limit systems (LLSs,  $17.2 \leq \log N_{\text{H I}} < 19$ ) that are mostly ionized, the damped Ly $\alpha$  absorbers (DLAs;  $\log N_{\text{H I}} \geq 20.3$ ) that are mostly neutral, and lastly the super-LLSs or sub-DLAs<sup>11</sup> for the intermediate category of absorbers with  $19 \leq \log N_{\text{H I}} < 20.3$ . Unlike absorbers at lower column densities, gas in the DLAs is mostly neutral. In fact, at all epochs since  $z \sim 5$ , the DLAs have contained most of the neutral gas that is poised to fuel star formation in galaxies (Wolfe et al. 2005).

## 1.3. Emission–Absorption Connection

Because the H I column density threshold of DLAs was set by the observed limit of 21 cm emission at the cutoff boundaries of nearby spiral disks (Wolfe et al. 1986), the DLAs were expected to arise from gas-rich galactic disks even at high redshifts. However, the emission counterparts (i.e., the DLA galaxies) of most DLAs have eluded detection. Among the limited detections in optical searches, it is found that the DLA galaxies are very faint ( $r \gtrsim 24$ ) and close ( $\sim 2''$ ) to the QSOs (e.g., Steidel & Hamilton 1992; Fynbo et al. 2008), making it difficult to measure their redshifts. To improve efficiency, searches of the emission counterparts of DLAs have focused on DLAs that are clearly chemically enriched ( $[\text{M}/\text{H}] > -0.7$ ) (e.g., Fynbo et al. 2013; Jorgenson & Wolfe 2014) or sightlines that pass through multiple DLAs (e.g., Srianand et al. 2016). But still, only 16  $z > 1.9$  DLA host galaxies have been identified via emission lines in the optical (see Krogager et al. 2017; Møller & Christensen 2020, for compilations) over an extensive search period of nearly three decades. The advent of (sub)millimeter interferometers such as the Atacama Large Millimeter/submillimeter Array (ALMA) and the Expanded Very Large Array has significantly improved the success rate of identifying absorption-selected galaxies, because (1) the contrast between DLA host galaxies and the QSO is more favorable at longer wavelengths, and (2) the interferometers have an unattenuated view over a wide field of view (and thus do not require lucky slit placements). In only a few years, there have been four  $z \sim 4$  DLA galaxies identified

<sup>9</sup> Although most of the difference in  $\tau_{\text{dep}}$  is driven by the conversion factor from CO to molecular gas ( $\alpha_{\text{CO}} \equiv M_{\text{mol}}/L_{\text{CO}}$  in units of  $M_{\odot}/(\text{K km s}^{-1} \text{ pc}^2)$ ), constraints from dynamical masses and dust masses have shown that SMGs indeed have lower  $\alpha_{\text{CO}}$  than normal star-forming galaxies (e.g., Hodge et al. 2012; Magnelli et al. 2012a; Xue et al. 2018) and that the value adopted from local ultraluminous IR galaxies (ULIRGs,  $\alpha_{\text{CO}} = 1.0$ ; Downes & Solomon 1998; Papadopoulos et al. 2012) is more appropriate for SMGs than the Galactic value ( $\alpha_{\text{CO}} = 4.3$ ; Bolatto et al. 2013).

<sup>10</sup> Column densities are given in units of  $\text{cm}^{-2}$  throughout the paper.

<sup>11</sup> The two terms have been used interchangeably.

in [C II] 158  $\mu\text{m}$  (Neeleman et al. 2017, 2019) and five  $z \sim 2$  DLAs in CO(4–3) and CO(3–2) (Kanekar et al. 2020). Interestingly, the DLA galaxies previously identified in the optical/near-IR are not detected in CO and vice versa (Kanekar et al. 2020), indicating that observations at different wavelength are complementary to one another and that selection of HI absorption tags gas-rich galaxies of all types. Some DLAs also have multiple emission counterparts that are consistent with the absorption redshifts, suggesting a group/cluster environment (e.g., Fynbo et al. 2018).

The opposite approach to the searches of DLA galaxies is to start from an emission-selected galaxy sample and look for corresponding absorption lines in the spectra of nearby background QSOs. This approach requires chance alignments of foreground galaxies and background QSOs, and thus requires large samples of both populations. The implicit assumption is that the emission-selected galaxies have similar CGM properties, and therefore the absorption signals obtained from different galaxy–QSO pairs can be combined to provide meaningful average properties of a typical halo in the studied galaxy population. The searches for absorbers are no longer limited to DLAs, but apply to all optically thick absorbers (i.e., LLSs and sub-DLAs). At  $z \gtrsim 2$ , the targeted galaxy populations have included Lyman break galaxies (LBGs) (e.g., Simcoe et al. 2006; Rudie et al. 2012, 2013; Crighton et al. 2013, 2015) and QSOs (e.g., Hennawi et al. 2006; Prochaska et al. 2013b; Lau et al. 2016). In addition, using a sample of projected QSO pairs where one of the QSOs intercepts a DLA, Rubin et al. (2015) have probed the CGM of the DLA galaxy without identifying that galaxy in emission. These studies have mapped out the HI column density, the ion ratios, and the metallicity as functions of impact parameter ( $R_{\perp}$ ). The covering fraction of optically thick HI absorbers increases from  $\sim 30\%$  around LBGs (Rudie et al. 2012) and DLAs (Rubin et al. 2015) to  $\gtrsim 60\%$  around QSOs (Prochaska et al. 2013b) for sightlines out to  $R_{\perp} = 100\text{--}200$  kpc (comparable to the virial radius of DM halos with  $M_{\text{halo}} = 10^{12.5} M_{\odot}$  at  $z = 2$ :  $R_{\text{vir}} = 154$  kpc). The abundance of neutral gas in the halos of QSOs is particularly puzzling. Simulations predict that such massive halos are dominated by a hot  $T \sim 10^7$  K virialized plasma and a significantly lower covering factor of optically thick HI absorbers (e.g., Faucher-Giguère et al. 2015).

The unexpectedly large covering factor of LLSs around  $z \sim 2$  QSOs and the difficulty of reproducing the SMG population in galaxy formation models could both be symptoms of the same problem. Attempting to reduce this tension between observations and theory, more recent cosmological zoom-in simulations have implemented recipes of stronger and presumably more realistic stellar feedback, which manage to preserve cool gas reservoirs in the accreted subhalos during earlier phases of star formation before their infall into the massive halo. The presence of these gas-rich subhalos increases the covering factor of cool gas around QSOs (Faucher-Giguère et al. 2016), and their prolonged bombardment of the central galaxy leads to a rising star formation history that eventually produces SMGs in the range  $2 < z < 3$  (Narayanan et al. 2015; Lovell et al. 2021).

#### 1.4. Organization

QSO absorption-line spectroscopy combined with efficient emission-line mapping provides a powerful method to link star-forming galaxies with the neutral gas reservoir that may fuel

future star formation. Our understanding of the formation and evolution of massive galaxies is severely limited by the lack of observational constraints on the CGM of SMGs. The advent of Herschel large-scale far-infrared surveys has provided an opportunity to use projected SMG–QSO pairs to probe the CGM of SMGs. In this paper, we focus on one particularly interesting system—GAMA J0913–0107—where two background QSOs have revealed an unusually HI-rich CGM around a luminous SMG.

The main text of the paper is organized as follows. We first provide an orientation of the system in Section 2, then proceed with a detailed study of the emission sources (Section 3) and the absorption-line systems (Section 4), before finally drawing connections between the absorbers and their emission counterparts in Section 5. We conclude the paper with a summary of the main results and a discussion of the implications in Section 6. To keep the main text focused on the SMG–DLA system at  $z \approx 2.67$ , we move additional material to the Appendices. We analyze the optical source near the SMG and its potential lensing effect in Appendix A, present the methodology and result of our blind search of line emitters in the ALMA band-3 data in Appendix B, give an inventory of the line-of-sight contaminating absorbers at other redshifts in Appendix C, provide tables of detailed ionic column density and metallicity measurements in Appendix D, and describe our attempt to detect CO emission from faint optical sources near QSO1 and the identification of Comp b in Appendix E.

Throughout this paper, we adopt a model optimization method that combines a heuristic  $\chi^2$  minimization algorithm with a Markov Chain Monte Carlo (MCMC) algorithm (hereafter, the “AMOEBa + MCMC” method). It begins with using the downhill simplex method AMOEBa (Press et al. 1992) with simulated annealing AMOEBa\_SA to find the solution that minimizes the residual. Although computationally more expensive than other least- $\chi^2$  solvers (e.g., the Levenberg–Marquardt technique), AMOEBa\_SA has the advantage of avoiding being trapped in local minima in a multidimensional parameter space. This advantage is particularly important in more complex problems such as fitting the HI absorption profiles with many Voigt profiles (Section 4.2). Next, starting from the minimum- $\chi^2$  solution of AMOEBa\_SA, we use the differential evolution MCMC algorithm (Ter Braak 2006) implemented in EXOFAST\_DEMC (Eastman et al. 2013, 2019) to obtain the final solution and the statistical uncertainties of the parameters. The EXOFAST\_DEMC routine first determines the stepping scale of each parameter by varying it from the minimum  $\chi^2$  solution until  $\chi^2$  increases by one. It then starts the chains from positions that are randomly offset from the minimum  $\chi^2$  solution. The routine stops when the chains are considered well-mixed and the steps in the initial “burn-in” phase are removed. The marginalized  $1\sigma$  confidence interval of each parameter is determined from the values at the 15.8 and 84.1 percentiles of the concatenated chains, and the *median* values are adopted as the *formal* solution. Parameters derived from the model parameters are treated likewise: their formal values and uncertainties are calculated from the 50, 15.8, and 84.1 percentiles of the array directly calculated from the chains of model parameters.

We assume the  $\Lambda$ CDM cosmology with  $\Omega_{\text{m}} = 0.3$ ,  $\Omega_{\Lambda} = 0.7$ , and  $h \equiv H_0/(100 \text{ km s}^{-1} \text{ Mpc}^{-1}) = 0.7$  and quote proper/physical distances.

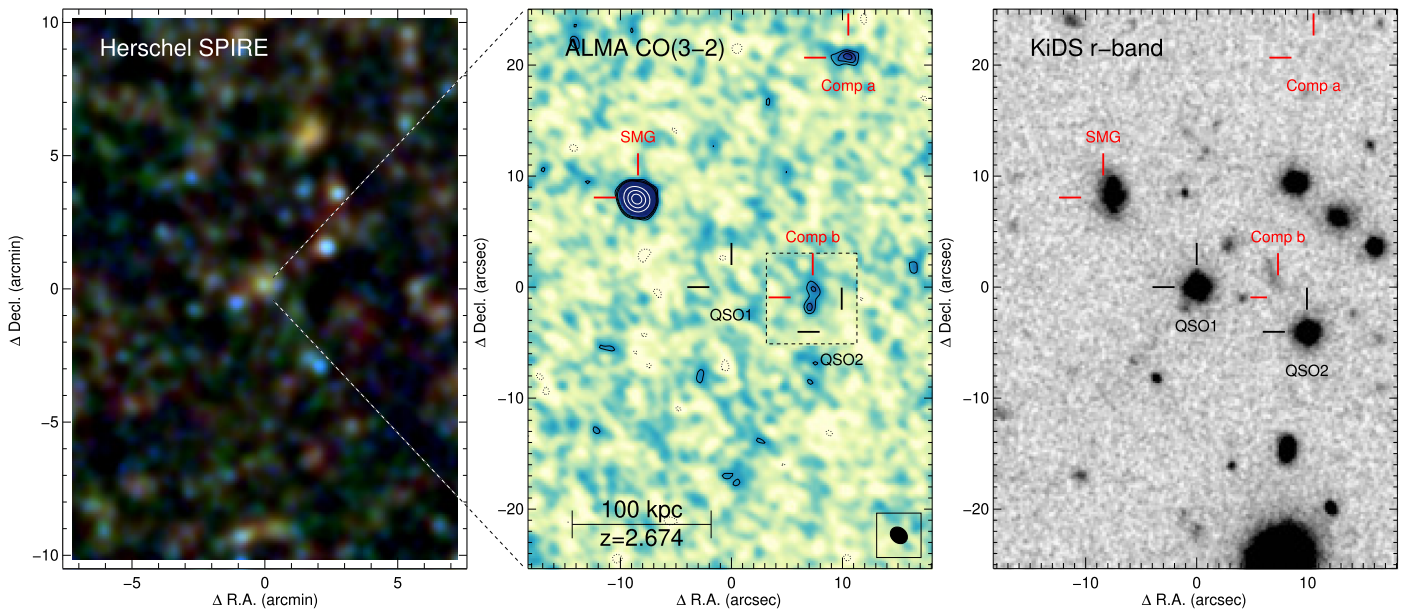


**Figure 1.** Multiwavelength images of the GAMA J0913–0107 system. Left: a wide-field Herschel pseudo-color image combining 250  $\mu\text{m}$  (blue), 350  $\mu\text{m}$  (green), and 500  $\mu\text{m}$  (red) images. The SMG is the bright source near the center of the  $15''.2 \times 21''.0$  region. Middle: an ALMA map zoomed in on the SMG, showing CO(3–2) emission in the range  $2.67 < z < 2.70$ . This  $36''.5 \times 50''.4$  region encloses the SMG and its CO companion galaxies (red tickmarks), and the two QSOs in the background of the system (black tickmarks). This composite CO image is formed by combining the 11 channels within  $\pm 140 \text{ km s}^{-1}$  of  $z = 2.674$  (i.e.,  $\nu_{\text{obs}} = 94.120 \pm 0.039 \text{ GHz}$ ). To show the CO emission from Comp b, the  $8'' \times 8''$  region centered on Comp b (dotted box) is formed by combining the two channels where CO emission is detected ( $\nu_{\text{obs}} = 93.7535$  and  $93.6676 \text{ GHz}$ , corresponding to  $z = 2.6884$  and  $2.6917$ ). The contours are drawn at  $-3$  (black dotted), 3, 4, 5 (black solid), 20, 40, and  $60\sigma$  (white solid). The synthesized beam of  $1''.6 \times 1''.3$  is shown in the lower right corner. Right: a deep  $r$ -band image of the same region from KiDS ( $5\sigma$  detection limit at  $\sim 25 \text{ mag}$ ). In all images, the position of QSO1 sets the origin of the coordinates.

**Table 1**  
Major Components of the GAMA J0913–0107 System and Impact Parameters

Designation	Short Name	R.A. (J2000) (deg)	Decl. (J2000) (deg)	$z$	$L'_{\text{CO}(3-2)}$ ( $\text{K km s}^{-1} \text{ pc}^2$ )	$\theta_1$ (arcsec)	$\theta_2$ (arcsec)	$R_{\perp,1}$ (kpc)	$R_{\perp,2}$ (kpc)
ALMA J091339.55–010656.4	SMM J0913	138.4147767	−1.1156772	2.674	$6.5 \times 10^{10}$	11.7	22.1	93.1	175.5
ALMA J091338.28–010643.8	Comp a	138.4094849	−1.1121639	2.6747	$6.3 \times 10^9$	23.3	24.8	185.1	197.1
ALMA J091338.49–010705.5	Comp b	138.4103803	−1.1181869	2.6884	$6.8 \times 10^8$	7.4	4.1	58.9	32.2
...	...	...	...	2.6917	$5.3 \times 10^8$	...	...	...	...
SDSS J091338.97–010704.6	QSO1	138.4124260	−1.1179280	2.9161	...	...	...	...	...
SDSS J091338.30–010708.6	QSO2	138.4096520	−1.1190520	2.7488	$5.6 \times 10^9$	10.8	...	85.0	...

**Note.** QSO coordinates are from the KiDS DR4 catalog, the SMG coordinates are from the higher-resolution ALMA band-6 image, and the coordinates of Comp a and Comp b are from their CO emission detected in the ALMA band-3 data cube. Comp b has two rows because it is a superposition of two CO emitters likely involved in a merger. The quoted redshift of QSO2 is from the CO(3–2) line, which is slightly off from its optical redshift ( $z_{\text{opt}} = 2.7498$ ,  $\delta v = 80 \text{ km s}^{-1}$ ). The column  $L'_{\text{CO}(3-2)}$  lists the CO(3–2) line luminosities from ALMA. The CO emission of QSO1 is outside our spectral coverage. The columns  $\theta_1$  and  $\theta_2$  list the angular separations from QSO1 and QSO2, respectively, and the corresponding transverse proper distances at the source redshift (i.e., the impact parameters) are listed as  $R_{\perp,1}$  and  $R_{\perp,2}$ .

## 2. System Overview

Figure 1 illustrates the GAMA J0913–0107 system, where we label its major components: the SMG, its CO companions, and the two background QSOs. Table 1 lists their coordinates, redshifts, and CO(3–2) luminosities, along with the impact parameters of the QSO sightlines.

The GAMA J0913–0107 system is one of the 163 SMG–QSO pairs with apparent separations between  $5''$  and  $30''$ , which were selected by cross-matching Herschel-selected SMGs with optically selected QSOs from a compilation of spectroscopic surveys (Fu et al. 2016, 2017). Located in the R.A. = 9 hr equatorial field of the Herschel Astrophysical Terahertz Large Area Survey (H-ATLAS) (Eales et al. 2010), the Herschel source at R.A. =  $09^{\text{h}}13^{\text{m}}39^{\text{s}}$ , decl. =  $-01^{\circ}06'59''$  is detected at high signal-to-noise ratio (S/N) by the Spectral and Photometric Imaging Receiver (SPIRE; Griffin et al. 2010)

at 250, 350, and 500  $\mu\text{m}$ , with de-boosted flux densities of  $S_{250} = 52.5 \pm 7.4 \text{ mJy}$ ,  $S_{350} = 69.4 \pm 8.8 \text{ mJy}$ , and  $S_{500} = 48.4 \pm 9.2 \text{ mJy}$  (Valiante et al. 2016; Fu et al. 2017). The far-IR SED clearly peaks around 350  $\mu\text{m}$  (i.e., “350  $\mu\text{m}$  peakers”), giving a rough photometric redshift of  $\sim 2.5$  assuming a dust temperature of  $\sim 50 \text{ K}$ , following Wien’s displacement law for  $S_\nu$  over  $\lambda$ :  $\lambda_{\text{peak}} = 102 \mu\text{m} \times (50 \text{ K}/T) (1 + z)$ .

Our ALMA 345 GHz imaging pinpointed the position of the Herschel source (Fu et al. 2017), and Gemini near-IR and ALMA 94 GHz spectroscopy jointly determined a spectroscopic redshift of 2.674 (Section 3.1 and 3.2). We designate the SMG as ALMA J091339.55–010656.4 or SMM J0913 for short. In addition, our ALMA 94 GHz observations detected companion galaxies in CO(3–2) near the redshift of the SMG: Comp a at  $z = 2.6747$  and Comp b at  $z = 2.6884, 2.6917$ . Both are within  $23''$  of the SMG position. Comp b has two redshifts

because it is a superposition of two galaxies (see Section 3.5). Because Herschel has FWHM resolutions of  $18''$ ,  $25''$ , and  $35''$  at 250, 350, and  $500\ \mu\text{m}$ , respectively, the SMG and its companions are blended in the Herschel images. But the contribution of the companions to the Herschel fluxes should be negligible given their orders-of-magnitude lower CO line luminosities.

There are two bright QSOs within  $22''$  of the SMG, QSO1 (SDSS J091338.97–010704.6,  $g = 20.78$ ,  $r = 20.38$ ) at  $z = 2.9161$  and QSO2 (SDSS J091338.30–010708.6,  $g = 20.71$ ,  $r = 20.44$ ) at  $z = 2.7488$ . Both are in the background of the SMG, allowing us to probe its CGM at impact parameters of  $R_{\perp} = 93.1$  kpc and  $R_{\perp} = 175.5$  kpc, or approximately  $0.5\times$  and  $0.9\times$  the virial radius of a  $10^{13}M_{\odot}$  halo at  $z = 2.674$  ( $R_{\text{vir}} = 186$  kpc). Coincidentally, strong HI and metal absorption lines near the SMG redshift have been previously detected in the QSO spectra (Finley et al. 2014).

When comparing the CO map with the Kilo-Degree Survey (KiDS)  $r$ -band image in Figure 1, we notice an  $r = 21.6$  optical source just  $0''.8$  from the SMG. As we will show in Appendix A, it is a foreground galaxy with a spec- $z$  of  $z = 0.055$  and its gravitational lensing effect on the SMG is negligible. We also find that Comp b is just  $\sim 3''$  from an elongated optical source to the NNE. In the KiDS DR4 catalog, the optical source has a designation of J091338.527–010703.60 and magnitudes of  $r = 23.8 \pm 0.1$  and  $H = 22.0 \pm 0.3$ . It has a photo- $z$  of  $z_p = 0.79^{+0.45}_{-0.06}$ . Its SED shows a clear drop-off of one magnitude between the  $Y$  band and  $Z$  band, corresponding to a  $4000\ \text{\AA}$  break at  $z \sim 1.2$ – $1.5$ , which is consistent with the maximum-likelihood photo- $z$  of  $z_p = 1.37$  in the catalog. We thus conclude that the optical source is most likely a foreground galaxy, although the extraction of an ALMA spectrum near the position of the optical source led to the identification of Comp b (Appendix E).

### 3. The Submillimeter Galaxy and Its Companions

#### 3.1. ALMA Position and Near-IR Spectroscopy

Herschel/SPIRE positions have large uncertainties. A comparison between ALMA and Herschel positions showed a  $1\sigma$  positional offset of  $\sim 4''.2$  for sources with  $S/N \sim 6$  at  $250\ \mu\text{m}$  (Equation (5) of Fu et al. 2017). Near-IR slit spectroscopy requires subarcsecond positions, so we carried out  $0''.5$  resolution ALMA band-7 ( $345\ \text{GHz}/870\ \mu\text{m}$ ) observations of GAMA J0913–0107 as part of our Cycle 3 project 2015.1.00131.S (see Fu et al. 2017, for details). GAMA J0913–0107 shared an hour-long observing session with nine other Herschel SMGs in the same H-ATLAS field. With four scans and 44 antennas, we accumulated a total on-source integration time of 189.5 s. A single source with high  $S/N$  is detected in the  $\sim 17''$  full width at half power (FWHP) of the primary beam. It has a  $870\ \mu\text{m}$  flux density of  $S_{870} = 7.4 \pm 0.5$  mJy, an offset from the Herschel position of  $4''.1$ , and a beam-deconvolved FWHM of  $0''.46 \pm 0''.04$  along the major axis (which corresponds to  $\sim 4$  kpc at  $z = 2.5$ ).

The accurate ALMA position enabled our follow-up near-IR slit spectroscopy. Observations of SMM J0913 were carried out with the Gemini near-infrared spectrograph (GNIRS; Elias et al. 2006) on 2017 February 19 as part of our queue program GN-2017A-Q-31. The A0-type star HIP49125 ( $V = 7.19$ ,  $K = 6.553$  Vega mag) was observed right after the science target to provide telluric correction and flux calibration.

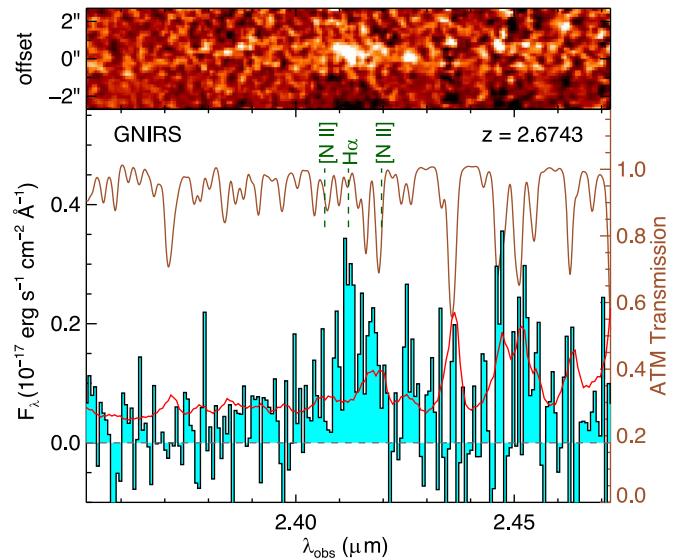


**Figure 2.** The GNIRS near-IR spectrum of SMM J0913. The top panel shows the coadded 2D spectrum. The ordinate is the positional offset along the spatial direction and is centered on the SMG location. The bottom panel shows the flux-calibrated 1D spectrum (black) and its  $1\sigma$  uncertainty (red). Wavelengths affected by strong sky lines show large errors. The dashed lines indicate the redshifted  $H\alpha$  and  $[N\ II]\ \lambda\lambda\ 6550, 6585$  lines. The brown curve shows the atmospheric transmission curve, using the ordinate on the right.

Because our goal was to measure the redshift, we used the cross-dispersed mode with the  $32\ \text{line}\ \text{mm}^{-1}$  grating to achieve a continuous wavelength coverage between  $0.85$  and  $2.5\ \mu\text{m}$  (orders 3 to 8). After applying a  $30''$  offset from an offset star to the NE, we placed the  $1''$  wide,  $7''$  long slit on the ALMA  $870\ \mu\text{m}$  position at a position angle (PA) of  $73^\circ$  (E of N; the PA was chosen to reach a guide star). The expected spectral resolution of this configuration is  $R = 510$  ( $\text{FWHM} = 590\ \text{km}\ \text{s}^{-1}$ ), but the actual spectral resolution may be higher depending on the source size and the seeing. We took 24 exposures of 136 s with an ABBA dithering pattern using a  $3''$  step. Data reduction was performed with a modified version of Spextool (Cushing et al. 2004) for GNIRS by K. Allers. The final coadded spectrum in Figure 2 includes all 24 frames and has a total on-source time of 54.4 minutes. We detected an emission line at  $\sim 4\sigma$  level at  $2.4121\ \mu\text{m}$  (heliocentric-corrected, vacuum wavelength), which we identified as  $H\alpha$  ( $\lambda_{\text{rest}} = 6564.63\ \text{\AA}$ ) at  $z_{H\alpha} = 2.6743 \pm 0.0003$ . The  $[N\ II]\ \lambda 6585.28$  line is undetected, likely due to the elevated background noise at its wavelength and its lower flux. Our best-fit Gaussian model yields a line  $\text{FWHM} = 230 \pm 60\ \text{km}\ \text{s}^{-1}$  (i.e., the line is unresolved) and a line flux of  $F_{H\alpha} = (6.1 \pm 1.0) \times 10^{-17}\ \text{erg}\ \text{s}^{-1}\ \text{cm}^{-2}$ , which are comparable to those of the SMGs identified by the Very Large Array (VLA; Alaghband-Zadeh et al. 2012; Fu et al. 2016).

#### 3.2. ALMA CO(3–2) Spectral Line Imaging

To detect the molecular gas reservoir that fuels the intense star formation in the SMG, we carried out deep ALMA band-3 ( $100\ \text{GHz}/3\ \text{mm}$ ) spectral line observations of SMM J0913 on 2018 December 10 and 15 with our Cycle 6 project 2018.1.00548.S. We tuned the four  $1.875\ \text{GHz}$  bandwidth spectral windows to center on  $92.2$  (BB3),  $94.0$  (BB4),  $104.2$  (BB1), and  $106.0\ \text{GHz}$  (BB2) in dual linear polarization mode

(*XX* and *YY*). We chose a spectral averaging factor of 16 to bin the frequency division mode (FDM)’s input channel spacing of 0.488 MHz to an output channel spacing of 7.8125 MHz. The spectral averaging significantly reduces the output data rate and essentially eliminates the correlation between adjacent channels introduced by the Hanning window function applied to the correlation functions (see Section 5.5 in the ALMA Technical Handbook). The resulting spectral response function is basically a top-hat function with a width of 7.8125 MHz (i.e., the output channel spacing), which corresponds to a spectral resolution of 22–25 km s<sup>-1</sup>. The two lower-frequency spectral windows provide a continuous frequency range between 91.27 and 94.94 GHz, which covers the CO(3–2) line ( $\nu_{\text{rest}} = 345.79599$  GHz and  $\lambda_{\text{rest}} = 866.96337$   $\mu\text{m}$ ) in the range  $2.642 \leq z \leq 2.789$ , encompassing the SMG at  $z = 2.674$  and QSO2 at  $z = 2.7498$ . The frequency range covers a velocity window between  $-2620$  and  $+9240$  km s<sup>-1</sup> relative to the SMG redshift. The two higher-frequency spectral windows provide a continuous frequency coverage between 103.27 and 106.94 GHz, which covers the CO(3–2) line in the range  $2.234 \leq z \leq 2.348$  and traces the continuum emission at rest-frame frequencies around  $\nu_{\text{rest}} = 386$  GHz ( $\lambda_{\text{rest}} = 776$   $\mu\text{m}$ ) at  $z = 2.674$ .

The primary beam of the ALMA 12 m antennas has an FWHP of 62'' at 94 GHz. We set the field center at R.A. = 09<sup>h</sup>13<sup>m</sup>38<sup>s</sup>.89, decl. =  $-01^{\circ}07'03''.6$ , which is near the position of QSO1 but  $\sim 12''$  offset from the SMG. Three of the four planned observing sessions were executed, accumulating a total on-source time of 143.8 minutes with 6.05 s integrations. Either 43 or 46 12 m antennas were operational, with baselines ranging between 15.1 m and 740.5 m. The BL Lac object J0854+2006 served as the amplitude, bandpass, and pointing calibrator, and the flat-spectrum radio quasar J0909+0121 as the phase calibrator (Bonato et al. 2019).

### 3.3. ALMA Data Processing

The raw visibility data were flagged and calibrated by the ALMA pipeline (Pipeline ver. 42030M, CASA ver. 5.4.0–68). The calibrated visibilities of the three observing sessions were then combined to form the final calibrated measurement set (MS). The pipeline worked very well. After inspecting the amplitudes of the calibrated visibilities, we found that additional flagging was only necessary for a tiny fraction of data. We used the CASA task `flagcmd` to flag the cross-correlation data of the antenna pair DA62 and DA65 in the 94.0 GHz spectral window between channels 188 and 191.

We use the CASA task `tclean` to image the calibrated visibilities of each spectral window into spectral data cubes. When visibilities are gridded into regularized *uv* cells, we adopt natural weighting to maximize the sensitivity. The synthesized beams are on average  $1''.7 \times 1''.3$  in FWHM, so we set the imaging pixel size to 0''.2. In the spectral dimension, we retain the original channel spacing of 7.8125 MHz. The data were recorded in the topocentric (TOPO) reference frame. Due to the motion of the Earth, every observing scan has a slightly different sampling in sky frequency. We image the data to the solar system barycenter (BARY) reference frame to be consistent with the velocities measured in the heliocentric-corrected optical and near-IR spectra.

Significant continuum emission and a strong emission line at  $\sim 94.1$  GHz (in BB4) are detected at the ALMA 870  $\mu\text{m}$  position of SMM J0913. To minimize the sidelobes from this

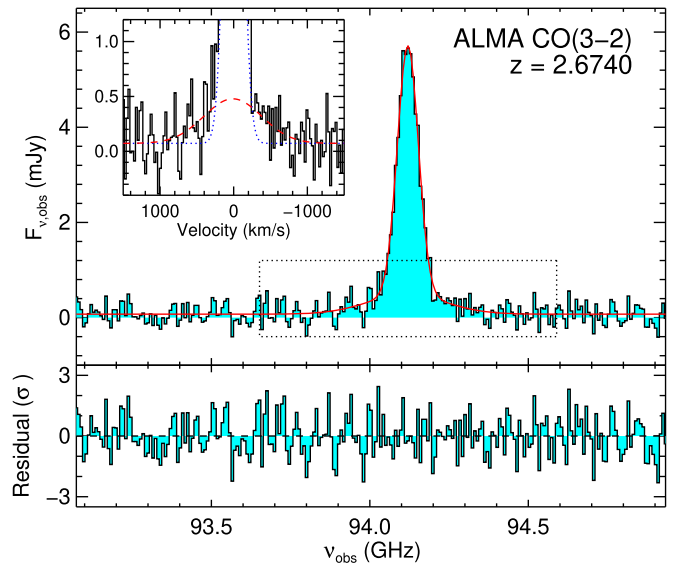


**Figure 3.** ALMA CO(3–2) spectrum of SMM J0913 and the best-fit double-Gaussian model (red solid curve). The inset shows a zoomed-in version of the spectrum to highlight the broad component (red dashed curve) beneath the narrow component (blue dotted curve). The dotted rectangle shows the portion of the spectrum shown in the inset. The bottom panel shows the residual (data – model) in units of  $1\sigma$  error.

bright source, we used the Clark CLEAN deconvolution algorithm with a mask consisting of a single circle of 2'' radius centered on the SMG. The CLEAN depth is set to be  $2\times$  the rms listed below.

For each spectral window, we generate two data cubes: one avoids interpolation in the spectral dimension by setting `interpolation = nearest` and is uncorrected for the primary beam, and the other uses linear interpolation and is corrected for the primary beam. The former is better suited for blind line searches because maps in adjacent channels remain uncorrelated, while the latter is better suited for measuring line parameters such as central frequency, width, and integrated flux. The resulting spectral cubes have a dimension of 540 pixels by 540 pixels by 240 channels. At the phase center, the sensitivities of the data cubes reach  $\text{rms} = 0.165, 0.171, 0.158,$  and  $0.155$  mJy beam<sup>-1</sup> channel<sup>-1</sup> for BB1, BB2, BB3, and BB4, respectively. The rms values are consistent with the visibility noise that we measured with `visstat` ( $\sigma \sim 250$  mJy visibility<sup>-1</sup> channel<sup>-1</sup>), because  $\text{rms} \sim \sigma / \sqrt{n_{\text{ch}} n_{\text{pol}} n_{\text{baseline}} n_{\text{int}}}$ , where  $n_{\text{ch}} = 1$  (one-channel binning),  $n_{\text{pol}} = 2$  (two polarizations),  $n_{\text{baseline}} = n_{\text{ant}}(n_{\text{ant}} - 1)/2 = 903$  for  $n_{\text{ant}} = 43$  (903 baselines for 43 antennae), and  $n_{\text{int}} = t_{\text{on\_source}}/t_{\text{int}} \sim 1426$  (total number of integrations).

In addition, we generate one continuum image from the two higher-frequency spectral windows (BB1 and BB2). We used the multiterm multifrequency synthesis (`mtmfs`) CLEAN algorithm with a linear spectral model (i.e., `nterms` = 2). Again, we used natural weighting, 0''.2 pixel size, and the same CLEAN mask centered on the SMG. The sensitivity of the continuum image reaches  $\text{rms} = 7.4$   $\mu\text{Jy beam}^{-1}$ , consistent with the rms of the spectral cubes divided by  $\sqrt{n_{\text{ch}}} \simeq 22$ .

### 3.4. SMG Properties

Figure 3 shows the ALMA band-3 spectrum of the SMG. The spectrum is extracted with an elliptical aperture matching the beam-convolved source size. A prominent emission line peaks at  $\nu_{\text{obs}} = 94.12$  GHz, which we identify as the CO(3–2)

**Table 2**  
Spectroscopy of the SMG

Quantity	Measurement	Unit
H $\alpha$ from Gemini/GNIRS		
$z_{\text{H}\alpha}$	2.6743(3)	...
$\Delta V_{\text{FWHM}}$	<300	km s $^{-1}$
$F_{\text{H}\alpha}$	$(6.1 \pm 1.0) \times 10^{-17}$	erg s $^{-1}$ cm $^{-2}$
$L_{\text{H}\alpha}$	$(2.9 \pm 0.5) \times 10^{41}$	erg s $^{-1}$
$\text{SFR}_{\text{H}\alpha}$	$1.6 \pm 0.3$	$M_{\odot}$ yr $^{-1}$
CO(3–2) from ALMA Band 3		
<i>Narrow Component</i>		
$z_{\text{CO}3-2}$	2.67399(3)	...
$\Delta V_{\text{FWHM}}$	$249 \pm 8$	km s $^{-1}$
$S_{\text{CO}}\Delta V$	$1.38 \pm 0.06$	Jy km s $^{-1}$
$L'_{\text{CO}3-2}$	$(5.0 \pm 0.2) \times 10^{10}$	K km s $^{-1}$ pc $^2$
<i>Broad Component</i>		
$z_{\text{CO}3-2}$	2.6741(7)	...
$\Delta V_{\text{FWHM}}$	$906 \pm 206$	km s $^{-1}$
$S_{\text{CO}}\Delta V$	$0.41 \pm 0.07$	Jy km s $^{-1}$
$L'_{\text{CO}3-2}$	$(1.5 \pm 0.3) \times 10^{10}$	K km s $^{-1}$ pc $^2$
<i>Total Emission</i>		
$L'_{\text{CO}1-0}$	$(1.25 \pm 0.07) \times 10^{11}$	K km s $^{-1}$ pc $^2$
$M_{\text{mol}}$	$(1.25 \pm 0.07) \times 10^{11}$	$M_{\odot}$
<i>Intrinsic Source Size</i>		
Deconv. Maj.	$0.76 \pm 0.09$	arcsec
Deconv. Min.	$0.54 \pm 0.17$	arcsec

**Note.** We have adopted a CO(3–2)/CO(1–0) brightness temperature ratio of  $r_{31} = 0.52$  and a conversion factor from CO to molecular gas of  $\alpha_{\text{CO}} \equiv M_{\text{mol}}/L'_{\text{CO}1-0} = 1.0 M_{\odot}/(\text{K km s}^{-1} \text{pc}^2)$ . Here and in Table 3, the intrinsic source sizes are given by the beam-deconvolved major- and minor-axis FWHMs ( $a$  and  $b$ ), measured by CASA task `imfit`.

line at  $z_{\text{CO}} = 2.67399 \pm 0.00003$ . The CO detection thus confirms the H $\alpha$  redshift from the GNIRS spectrum ( $z_{\text{H}\alpha} = 2.6743 \pm 0.0003$ , see Section 3.1). Because the CO line is detected at a higher S/N and is less affected by dust extinction, we adopt the CO redshift for the SMG throughout the paper, i.e.,  $z_{\text{SMG}} = z_{\text{CO}} = 2.674$  (a slightly rounded-up value for simplicity).

A closer inspection of the CO(3–2) spectrum reveals a broad (FWHM  $\sim 1000$  km s $^{-1}$ ) emission-line component with a peak flux of  $\sim 0.4$  mJy underneath the prominent narrow component (FWHM  $\sim 250$  km s $^{-1}$ ). We thus model the CO spectrum with two Gaussians and compare its result with a single-Gaussian model.

We find that the improvement of the double-Gaussian model over the single-Gaussian model is highly significant. The formal double-Gaussian solution achieves  $\chi^2 = 220.2$  for a degree of freedom (DOF) of 209. For comparison, the formal single-Gaussian solution achieves  $\chi^2 = 251.8$  for DOF = 212. According to the  $F$ -test, such a difference rejects the null hypothesis, that the double-Gaussian model does not provide a significantly better fit, at a confidence level of 99.99964% or  $4.6\sigma$ . The result of the double-Gaussian fit from the ‘‘AMOEBa + MCMC’’ method is listed in Table 2. The broad component has an FWHM of  $\sim 900$  km s $^{-1}$  and accounts for almost a quarter of the total emission-line flux. The existence of a narrow CO line on top of a broad CO line with essentially no velocity offset indicates that the SMG’s intense star-forming nucleus (the narrow component) is either embedded in a fast-

rotating disk or driving a bipolar outflow (the broad component). Unfortunately, the spatial resolution of the ALMA data is inadequate to distinguish between the two scenarios. We note that such a broad CO component would not have been detected in shallower spectroscopic data that are more generally available to SMGs, so this feature may not be unique to SMM J0913.

With the redshift determined, we fit the SED between 250  $\mu\text{m}$  and 3 mm from Herschel/SPIRE and ALMA with a modified blackbody curve. We adopt the general solution of the radiative transfer equation assuming local thermal equilibrium at a constant temperature  $T$ :

$$S_{\nu} = (1 - e^{-\tau_{\nu}}) B_{\nu}(T) \pi r_s^2 / d_L^2, \quad (3)$$

where  $B_{\nu}(T)$  is the Planck function at a temperature  $T$  and a rest-frame frequency  $\nu$ ,  $\pi r_s^2$  the effective size of the dust-emitting region, and  $d_L$  the luminosity distance. Assuming that the dust opacity follows a power law with a negative slope of  $-\beta$  at wavelengths greater than the dust size ( $\sim 10$   $\mu\text{m}$ ), the optical depth should follow the same power law:

$$\tau_{\nu} = (\nu/\nu_0)^{\beta} = (\lambda/\lambda_0)^{-\beta}, \quad (4)$$

where  $\nu_0$  ( $\lambda_0$ ) is the rest-frame frequency (wavelength) at which the dust becomes optically thick. Given the dust mass-absorption coefficient of  $\kappa = 0.07$  m $^2$  kg $^{-1}$  at 850  $\mu\text{m}$  for Galactic dust (Dunne et al. 2000; James et al. 2002), it can be shown that the dust mass is

$$M_{\text{dust}} = 9.0 \times 10^9 M_{\odot} (\pi r_s^2 / \text{kpc}^2) (\lambda_0 / 850 \mu\text{m})^{\beta}. \quad (5)$$

The result of the SED fit gives us a measure of the dust temperature, the dust-obscured SFR, the dust mass, and the effective size of the dust photosphere. Figure 4 (left) shows the multiband photometry, the median MCMC model, and the  $1\sigma$  spread of the models. Table 3 lists the formal parameters and their uncertainties. The dust is relatively warm ( $T = 44 \pm 7$  K) and the dust photosphere has an effective size of  $9_{-5}^{+10}$  kpc $^2$ , comparable to the intrinsic source size measured at 343.5 GHz —  $\pi ab/4 = 6.4 \pm 1.5$  kpc $^2$ .

The ALMA CO(3–2) line luminosity offers an estimate of the mass of the molecular gas reservoir. Because CO(3–2) traces the warm and moderately dense ( $n_{\text{eff}} \sim 10^4$  cm $^{-3}$ ) component (e.g., Juneau et al. 2009), we first convert the CO(3–2) to CO(1–0) luminosity using the average brightness temperature ratio of  $r_{31} \equiv L'_{\text{CO}3-2}/L'_{\text{CO}1-0} = 0.52$  observed in SMGs (Bothwell et al. 2013). We then convert the CO(1–0) luminosity to the total molecular gas mass with a conversion factor from CO to molecular gas of  $\alpha_{\text{CO}} = 1.0$ , a value found appropriate for high-redshift dusty starbursts (e.g., Hodge et al. 2012; Magnelli et al. 2012b; Xue et al. 2018). The result is a total molecular gas mass of  $M_{\text{mol}} = (1.25 \pm 0.07) \times 10^{11} (r_{31}/0.52)^{-1} (\alpha_{\text{CO}}/1.0) M_{\odot}$ , near the high end of the molecular gas masses measured in SMGs (see Figure 4 middle).

Combining the results from the SED fit and the CO(3–2) spectroscopy, we found a gas depletion timescale of  $\sim 0.1$  Gyr, which is similar to other SMGs but  $6\times$  shorter than for coeval main-sequence galaxies (Figure 4 middle). The SMG’s dust emission is resolved by the ALMA band-6 data with a beam-deconvolved size of  $0''.46 \times 0''.28$ . Its CO(3–2) emission is resolved by the ALMA band-3 data with a beam-deconvolved size of  $0''.76 \times 0''.54$ . In both cases, we have measured the intrinsic source sizes from CLEAN’ed images using the CASA

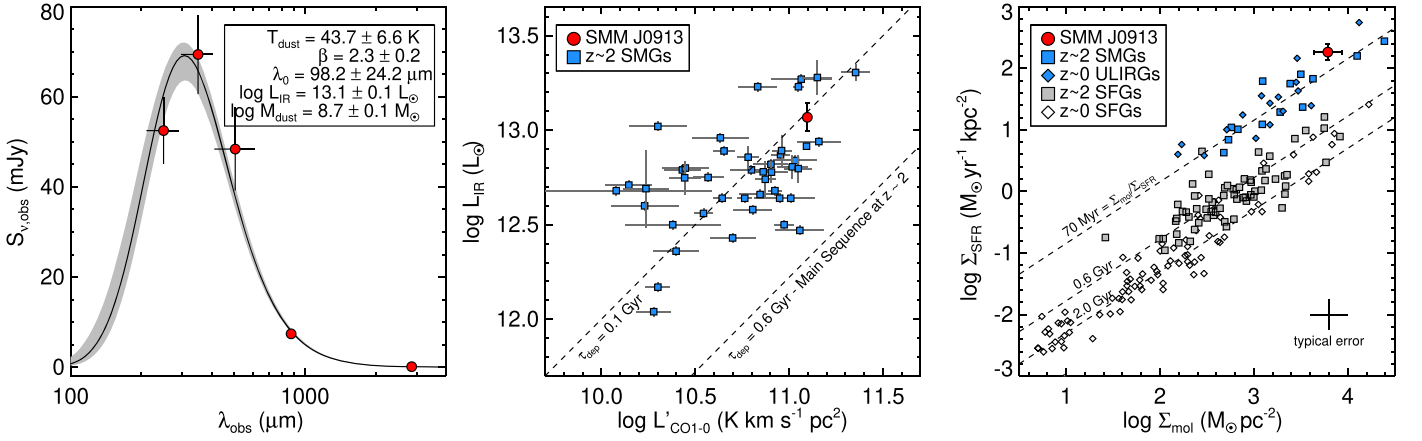


**Figure 4.** Physical properties of SMM J0913 (red data points). Left: the far-IR SED from Herschel and ALMA and the formal MBB solution. The shaded area shows the  $1\sigma$  spread of the models in the MCMC chains. Middle: CO(1–0) luminosity vs. IR luminosity. Blue squares show SMGs from the literature (Harris et al. 2010; Ivison et al. 2011; Riechers et al. 2011; Bothwell et al. 2013; Sharon et al. 2013). The dashed lines show contours of constant gas depletion timescales. Right: SFR surface density vs. molecular gas mass surface density (i.e., the Kennicutt–Schmidt relation). Other data points show local ULIRGs (Kennicutt 1998), high-redshift SMGs (Daddi et al. 2009; Genzel et al. 2010; Fu et al. 2013), and normal star-forming galaxies at  $z \sim 2$  and  $z \sim 0$  (Tacconi et al. 2013). The dashed lines indicate constant ratios of surface densities, which are another indicator of the gas depletion timescale.

**Table 3**  
Photometry of the SMG

Quantity	Measurement	Unit
Herschel/SPIRE		
R.A.	09:13:39.32	h:m:s
Decl.	−01:06:58.6	d:m:s
$S_{250}$	$52.5 \pm 7.4$	mJy
$S_{350}$	$69.4 \pm 8.8$	mJy
$S_{500}$	$48.4 \pm 9.2$	mJy
ALMA Band-6 Continuum		
R.A.	09:13:39.55	h:m:s
Decl.	−01:06:56.4	d:m:s
$S_{343.5 \text{ GHz}}$	$7.4 \pm 0.5$	mJy
Deconv. Maj.	$0.46 \pm 0.04$	arcsec
	$3.7 \pm 0.3$	kpc
Deconv. Min.	$0.28 \pm 0.06$	arcsec
	$2.2 \pm 0.5$	kpc
ALMA Band-3 Continuum		
$S_{93.1 \text{ GHz}}$	$106 \pm 22$	$\mu\text{Jy}$
$S_{105.1 \text{ GHz}}$	$111 \pm 20$	$\mu\text{Jy}$
Deconv. Maj.	$0.68 \pm 0.47$	arcsec
Deconv. Min.	$0.47 \pm 0.23$	arcsec
Modified Blackbody Fit		
$T$	$44 \pm 7$	K
$\beta$	$2.3 \pm 0.2$	...
$\lambda_0$	$98 \pm 24$	$\mu\text{m}$
$\pi r_s^2$	$9_{-5}^{+10}$	$\text{kpc}^2$
$M_{\text{dust}}$	$(5.4 \pm 1.2) \times 10^8$	$M_\odot$
$L_{\text{IR}}$	$1.17_{-0.11}^{+0.17} \times 10^{13}$	$L_\odot$
SFR <sub>IR</sub>	$1170_{-110}^{+170}$	$M_\odot \text{ yr}^{-1}$

**Note.** The errors of the Herschel photometry include confusion noises of 5.3, 6.4, and 6.7 mJy beam $^{-1}$  at 250, 350, and 500  $\mu\text{m}$ , respectively (Pascale et al. 2011; Rigby et al. 2011). The IR luminosity,  $L_{\text{IR}}$ , is defined as the integrated luminosity between 8 and 1000  $\mu\text{m}$  in the rest frame. The dust-obscured SFR is estimated using the commonly used conversion:  $\text{SFR}/M_\odot \text{ yr}^{-1} = 10^{-10} L_{\text{IR}}/L_\odot$  (e.g., Daddi et al. 2010).

task imfit. These size measurements allow us to place the SMG on the Kennicutt–Schmit relation (Figure 4 right). It is characterized by high surface densities of SFR and molecular gas even compared to the SMG population. But like other SMGs, it features a high star formation efficiency that is distinct from normal star-forming galaxies at  $z \sim 2$  (e.g., Daddi et al. 2010; Genzel et al. 2010).

### 3.5. Companion Galaxies

We carried out a blind search of line emitters in the ALMA data cubes with a matched-filter algorithm and tested the fidelity of the detections with simulated noise-only interferometer data (see Appendix B). In the spectral window centered at 94 GHz (i.e., BB4), we found two robust line emitters: the SMG at  $z = 2.674$  ( $S/N = 67$ ) and Comp a at  $z = 2.6747$  ( $S/N = 6.4$ ). The other companion, Comp b, was detected at high significance when we combined the two ALMA channels closest in velocity to the metal-line-detected absorbing clouds C1 and C2 toward QSO1 (see Section 4.3). The source has a peak  $S/N$  of 4.5 when combining the two channels, while its peak  $S/N$  is only 3.6 in the two individual channels, making it confused with noise spikes. The matched-filter algorithm fails to identify Comp b because it assumes that only adjacent channels can boost the  $S/N$  above the detection limit. In other words, the detection of Comp b is possible only because (1) we have utilized the prior knowledge of the redshifts of the absorption lines (with the implicit assumption that the emission counterparts have similar redshifts), and (2) the emission counterparts of the two clouds are superimposed on the sky (increasing the  $S/N$  when they are combined).

Our blind search detected four additional high-fidelity line emitters: QSO2 at  $z = 2.7488$  ( $S/N = 7.0$ ), its companion at  $z = 2.7392$  ( $\delta v = -770 \text{ km s}^{-1}$ ;  $S/N = 6.1$ ) located  $\sim 30''$  to the NE of QSO2, and two additional sources at  $z = 2.3452$  ( $S/N = 5.5$ ) and  $z = 2.3324$  ( $S/N = 5.2$ ) that may correspond to the  $z_{\text{abs}} = 2.345$  H I and C IV absorbers that appear toward both QSOs (see Figure C1 in Appendix C). But on the other hand, only the SMG is detected in the continuum image of the two higher-frequency spectral windows (i.e., BB1 and BB2).

While the detection of CO in the SMG and QSO2 is expected, the detection of their companion CO emitters is not. We can use the ALMA Spectroscopic Survey in the Hubble Ultra Deep Field (ASPECS; Decarli et al. 2019) to estimate a baseline level of source-detection probability in normal field environments. The ASPECS covers an area of  $4.6 \text{ arcmin}^2$  ( $\text{PB} \geq 0.5$ , where PB is a correction factor for the primary beam pattern) with 17 pointings in band 3 and a spectral range of 21 GHz (84–105 GHz) with five tunings. The rms sensitivity varies with frequency with a range between 0.12 and  $0.4 \text{ mJy beam}^{-1} \text{ channel}^{-1}$  for a channel spacing of 7.8 MHz (the same as ours). To provide a conservative estimate, we only count the seven sources detected at  $\text{S/N} > 6$  between 96 and 103 GHz (González-López et al. 2019), where  $\text{rms} \simeq 0.135 \text{ mJy beam}^{-1} \text{ channel}^{-1}$ . Only within this spectral range is ASPECS more sensitive than our data ( $\text{rms} \simeq 0.16 \text{ mJy beam}^{-1} \text{ channel}^{-1}$ ). This gives a source density of  $0.22 \pm 0.08 \text{ arcmin}^{-2} \text{ GHz}^{-1}$  in the field. Given that our ALMA observations cover an area of  $0.88 \text{ arcmin}^2$  where  $\text{PB} \geq 0.5$  and are  $\sim 20\%$  shallower, one would expect to identify less than  $0.36 \pm 0.14$  sources at  $\text{S/N} > 6$  over the 1.875 GHz bandwidth of a baseband, and only a third of these (i.e.,  $< 0.12 \pm 0.05$  sources) are expected to fall within  $\pm 0.3 \text{ GHz}$  ( $1000 \text{ km s}^{-1}$ ) of the main galaxies to be considered as companions. In other words, one would need to increase our survey area by  $> 8\times$  to detect a chance “companion” galaxy of the SMG or QSO2 in the field. Yet we have detected one  $\text{S/N} > 6$  companion within  $30''$  of each main galaxy. Our result thus indicates that both the SMG and QSO2 inhabit overdense environments, which is consistent with their purported large halo masses (Hickox et al. 2012).

In addition to the companion galaxies detected in CO emission, both the SMG and QSO2 are also associated with absorbers of high HI column density in the spectrum of a common background QSO (QSO1), as we will show in the next section.

#### 4. Absorption-line Systems

The two QSOs in the GAMA J0913–0107 system were first identified in the Sloan Digital Sky Survey (SDSS) DR9 quasar catalog (Pâris et al. 2012). The pair has a separation of only  $10''.8$ , and more importantly, two closely separated DLAs were immediately identified in the low-resolution SDSS spectrum of QSO1 (Noterdaeme et al. 2012b). The stronger DLA ( $\log N_{\text{HI}} \simeq 21.3$ ) at  $z_{\text{abs}} \simeq 2.75$  is associated with QSO2 at  $z = 2.7488$ , providing an important probe of the CGM around QSOs at an impact parameter of  $R_{\perp} = 85 \text{ kpc}$  (see Appendix C). The other DLA ( $\log N_{\text{HI}} \simeq 20.5$ ) at  $z_{\text{abs}} \simeq 2.68$  provides a window to probe the CGM of the SMG at  $z = 2.674$ , which is just  $11''.7$  from the QSO.

We searched the spectral databases with `specdb`<sup>12</sup> and found that the QSO pair had accumulated an excellent set of spectroscopic data from Gemini Multiobject Spectrograph (GMOS; Prochaska et al. 2013a), VLT/X-shooter (Finley et al. 2014), and Magellan Echellette Spectrograph (MagE; Rubin et al. 2015). Finley et al. (2014) noticed the strong coincident absorption at  $z_{\text{abs}} \simeq 2.68$  in the SDSS spectra of both QSOs, which motivated them to obtain the higher-resolution X-shooter spectra for a detailed analysis. The absorption structure toward both QSOs is resolved into three major

subsystems of variable metallicities and with a total velocity span of  $> 1700 \text{ km s}^{-1}$ . The observed kinematic and metallicity coherence across sightlines is remarkable, given the 86 kpc separation between the QSOs. The authors interpreted the system as a gaseous overdensity extended by 6 Mpc along the line of sight, which is suggestive of a clumpy filamentary structure that may eventually collapse and form a protocluster. They attributed the two main subsystems at lower velocities (A and B) to part of the IGM because of their low metallicity ( $[\text{Fe}/\text{H}] < -1.9$ ) and suspected that the third main subsystem (C) with  $[\text{Fe}/\text{H}] = -1.1$  is likely associated with a galaxy. Now with the detection of the SMG and its companion galaxies, we will use the coincident absorption-line system to characterize the CGM of these galaxies in Section 5. We will show that subsystems A and B are cool gas streams in the CGM of the SMG, and subsystem C is indeed associated with a galaxy (Comp b).

In this section, we present a reanalysis of the  $z_{\text{abs}} \simeq 2.68$  absorption system using a new reduction of the X-shooter spectra (Section 4.1). Finley et al. (2014) used `vpfit`<sup>13</sup> to fit Voigt profiles to the entire spectrum. Our approach is complementary to the `vpfit` analysis and our results show a good agreement with those presented in Finley et al. (2014). The main differences between the two analyses are:

1. We fit Voigt profiles to the HI Lyman series after masking out contaminating LYAF lines and quantify the statistical and systematic uncertainties of the model parameters using an MCMC algorithm (Section 4.2).
2. We measure the ionic column densities of metals with the apparent optical depth method (AODM; Section 4.3). This is a more direct and conservative technique than Voigt profile fitting using `vpfit`, because it relies only on equivalent width measurements and uses a straightforward method to detect line saturation.
3. We use ionic column density ratios to constrain the photoionization model for each cloud, which in turn provides the ionization correction factors necessary for metallicity estimates (Section 4.4).
4. We use the SMG to define the systemic redshift and adopt the solar abundance scale of Asplund et al. (2009).

##### 4.1. VLT X-shooter Spectroscopy

The X-shooter observations of the QSOs took place between 2013 March 31 and 2013 May 1 on the 8.2 m VLT/UT2 telescope (program ESO 089.A-0855; Finley et al. 2014). X-shooter uses three individual echelle spectrographs to cover a wide wavelength range between 0.3 and  $2.5 \mu\text{m}$  simultaneously (Vernet et al. 2011). Finley et al. (2014) estimated spectral resolutions of  $R \sim 6400$  ( $\text{FWHM} = 47 \text{ km s}^{-1}$ ) in the UVB arm ( $3000\text{--}5600 \text{ \AA}$ ),  $R \sim 11,000$  ( $27 \text{ km s}^{-1}$ ) in the VIS arm ( $5500 \text{ \AA} \text{--} 1 \mu\text{m}$ ), and  $R \sim 6600$  ( $45 \text{ km s}^{-1}$ ) in the near-IR arm ( $1\text{--}2.5 \mu\text{m}$ ). The total exposure times are 100 minutes for QSO2 and 310 minutes for QSO1. We downloaded the raw data from the ESO archive and reduced the data with the spectroscopy data reduction pipeline developed by George Becker.<sup>14</sup> The final 1D spectra were corrected for the  $0.2 \text{ \AA}$  ( $0.5 \text{ pixel}$ ) wavelength redshift of the spectra in the VIS arm noticed

<sup>12</sup> <https://github.com/specdb/specdb>

<sup>13</sup> <https://people.ast.cam.ac.uk/~rfc/vpfit.html>

<sup>14</sup> [ftp://ftp.ast.cam.ac.uk/pub/gdb/xshooter\\_reduce/](ftp://ftp.ast.cam.ac.uk/pub/gdb/xshooter_reduce/)

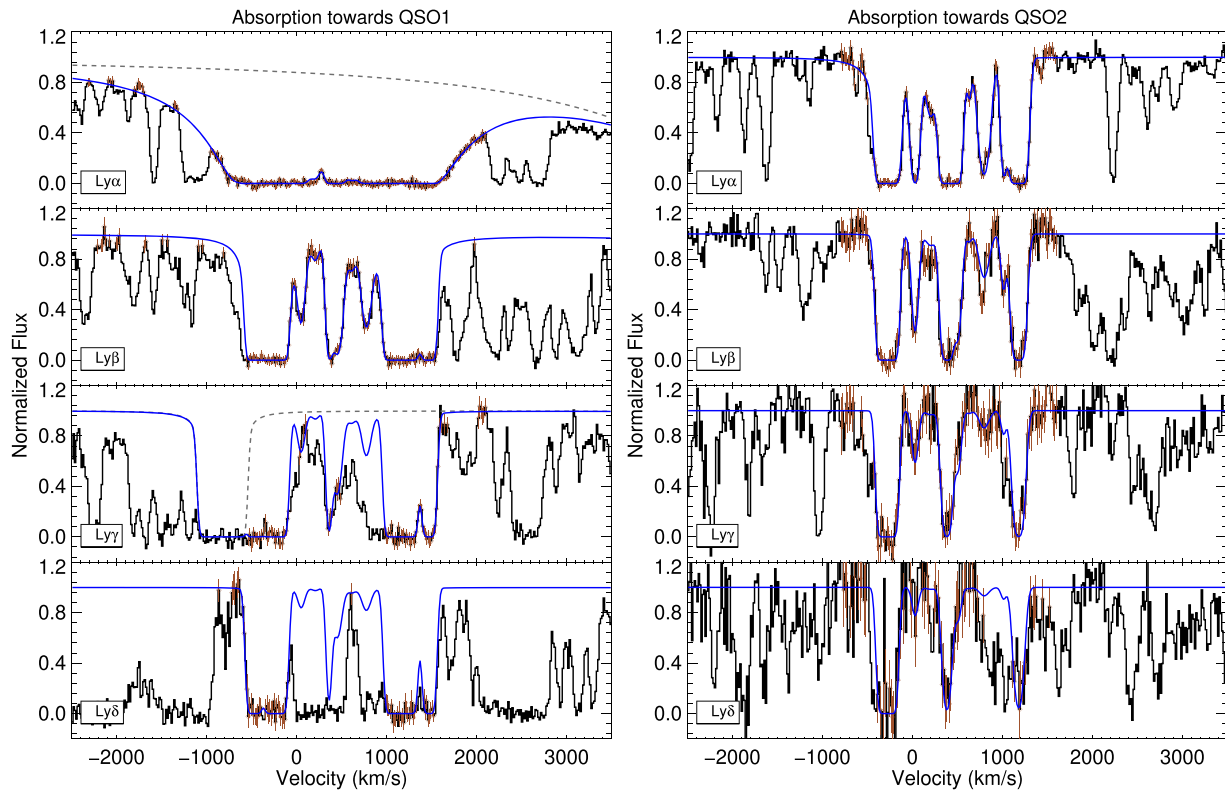


**Figure 5.** Velocity profiles of H I absorption near the SMG redshift toward QSO1 and QSO2, overlaid with best-fit Voigt profiles (blue curves). We indicate data points in contamination-free regions with brown diamonds with error bars. The gray dashed lines in the left panels show the H I Ly $\alpha$  and Ly $\delta$  absorption from the DLA at  $z_{\text{abs}} = 2.751$ ; note how significantly they affect the Ly $\alpha$  and Ly $\gamma$  profiles of the absorption at  $z_{\text{abs}} \approx 2.68$ . All velocities are relative to  $z_{\text{SMG}} = 2.674$ .

by Noterdaeme et al. (2012a), which is likely produced by uncompensated instrumental flexure.

We fit the QSO continuum using the Python software package `linetools`.<sup>15</sup> First, the spectrum is divided into a number of wavelength intervals, which are  $\sim 50$  Å wide shortward of the Ly $\alpha$  emission, narrower across strong emission lines, and wider in regions free of emission lines and longward of Ly $\alpha$ . Next, a spline is fit through the central wavelength and median flux of each interval (i.e., the spline “knots”). Finally, these “knots” are iteratively added, deleted, or moved until a satisfactory continuum fit is obtained.

#### 4.2. Voigt Profile Fitting of Neutral Hydrogen

Figure 5 shows the H I absorption profiles (Ly $\alpha$  through Ly $\delta$ ) of the absorbers at  $z_{\text{abs}} \approx 2.68$  toward the two QSOs. Although the two QSOs are separated by  $10''.8$  (86 kpc at  $z = 2.674$ ), their H I absorption profiles show strikingly similar velocity structures spanning over  $1800$  km s $^{-1}$ , as first noted by Finley et al. (2014). The kinematic coherence indicates that the medium responsible for the absorption extends at least 86 kpc across the sky plane.

Line blending from other absorbers is evident, as indicated by the disagreement in velocity profile among the Lyman series. To measure H I column densities in such a complex situation, it is beneficial to first identify a guessed solution by iteratively varying the Voigt profiles (convolved to  $R = 6400$ ) until an acceptable fit to the data is obtained. The guessed solution not only provides a good starting point for the

formal minimum  $\chi^2$  approach below, but also helps to identify regions contaminated by line blending (which thus should be flagged out). During this procedure, we find that a minimum of 10 clouds are needed to adequately fit the Lyman series in each sightline. Because each cloud is described by three parameters ( $v$ ,  $b$ ,  $\log N_{\text{HI}}$ ), our model for each QSO spectrum has a total of 30 free parameters.

To model the absorption toward QSO1, the H I Lyman lines of the DLA at  $z_{\text{abs}} \approx 2.751$  (see Figure C1(a)) must be included in the model because its Ly $\alpha$  and Ly $\delta$  blend with the Ly $\alpha$  and Ly $\gamma$  profiles of the absorber at  $z_{\text{abs}} \approx 2.68$ . We find that the DLA’s H I absorption is adequately modeled as two clouds separated by  $290$  km s $^{-1}$  ( $z_{\text{abs}} = 2.7502, 2.7538$ ), each with  $\log N_{\text{HI}} = 21.0$  and  $b = 40$  km s $^{-1}$  (see Figure C2). These parameters for the DLA at  $z_{\text{abs}} = 2.751$  are fixed in the fitting process.

The  $\chi^2$  minimization is focused on the velocity range between  $-1500$  and  $2100$  km s $^{-1}$  for QSO1 and between  $-600$  and  $1350$  km s $^{-1}$  for QSO2. With the guessed solution, we also mask out the pixels that are clearly contaminated by line blending within the fitting ranges. The surviving “good” pixels are indicated by diamond symbols with error bars in Figure 5 and the Voigt models are optimized using the AMOEBa + MCMC method described in Section 1.4. The priors of central velocities and column densities are centered around the guessed solution, with bounds of  $\pm 100$  km s $^{-1}$  for  $v_{\text{HI}}$  and  $\pm 0.8$  dex for  $\log N_{\text{HI}}$ . On the other hand, the Doppler parameter,  $b_{\text{HI}}$ , is allowed to vary between  $5$  and  $70$  km s $^{-1}$ . For three H I components, we found it necessary to fix their velocities to those measured from low-ion metal lines, because the H I series

<sup>15</sup> <https://github.com/linetools/linetools>

**Table 4**  
Voigt Solution for H I Lyman Lines

Toward QSO1			Toward QSO2		
$v_{\text{HI}}$ ( $\text{km s}^{-1}$ )	$b_{\text{HI}}$ ( $\text{km s}^{-1}$ )	$\log(N_{\text{HI}}/\text{cm}^{-2})$	$v_{\text{HI}}$ ( $\text{km s}^{-1}$ )	$b_{\text{HI}}$ ( $\text{km s}^{-1}$ )	$\log(N_{\text{HI}}/\text{cm}^{-2})$
$-470.1^{+0.0}_{-0.0}$	$32.2^{+1.0}_{-1.2}$	$19.64^{+0.04}_{-0.05}$	$-276.3^{+1.2}_{-1.3}$	$47.2^{+0.8}_{-0.7}$	$18.56^{+0.06}_{-0.09}$
$-224.7^{+0.0}_{-0.0}$	$42.2^{+0.6}_{-0.5}$	$20.06^{+0.04}_{-0.04}$	$-208.5^{+0.0}_{-0.0}$	$14.2^{+6.6}_{-6.3}$	$17.48^{+0.41}_{-0.47}$
$52.5^{+2.3}_{-2.4}$	$45.8^{+3.7}_{-3.6}$	$14.66^{+0.03}_{-0.03}$	$31.6^{+1.3}_{-1.3}$	$38.2^{+1.4}_{-1.4}$	$14.79^{+0.04}_{-0.04}$
$210.1^{+7.8}_{-8.2}$	$43.3^{+13.6}_{-12.0}$	$13.75^{+0.10}_{-0.11}$	$205.1^{+5.9}_{-5.9}$	$67.0^{+2.2}_{-4.2}$	$13.75^{+0.03}_{-0.03}$
$360.1^{+4.3}_{-3.4}$	$22.2^{+3.6}_{-3.5}$	$15.90^{+0.41}_{-0.25}$	$384.7^{+4.0}_{-4.2}$	$46.2^{+3.4}_{-3.6}$	$16.03^{+0.18}_{-0.13}$
$454.5^{+9.0}_{-8.1}$	$58.3^{+7.0}_{-8.3}$	$15.22^{+0.06}_{-0.07}$	$509.1^{+7.0}_{-8.4}$	$37.9^{+5.3}_{-4.6}$	$14.85^{+0.08}_{-0.08}$
$612.6^{+8.9}_{-9.4}$	$51.9^{+11.5}_{-11.4}$	$14.08^{+0.08}_{-0.08}$	$632.9^{+4.6}_{-4.8}$	$18.4^{+10.0}_{-7.9}$	$13.24^{+0.08}_{-0.07}$
$775.4^{+2.7}_{-2.7}$	$62.1^{+3.9}_{-3.9}$	$14.83^{+0.02}_{-0.02}$	$798.1^{+1.5}_{-1.5}$	$67.4^{+1.7}_{-2.1}$	$14.41^{+0.02}_{-0.02}$
$1159.5^{+2.0}_{-2.0}$	$59.0^{+0.7}_{-0.7}$	$20.23^{+0.02}_{-0.02}$	$1014.4^{+2.4}_{-2.3}$	$29.4^{+2.8}_{-2.6}$	$14.30^{+0.06}_{-0.05}$
$1474.8^{+1.6}_{-2.2}$	$30.2^{+1.0}_{-0.8}$	$18.79^{+0.14}_{-0.19}$	$1181.8^{+1.9}_{-1.9}$	$54.1^{+2.0}_{-2.0}$	$16.00^{+0.10}_{-0.09}$

**Note.** All velocities are relative to the SMG redshift ( $z_{\text{SMG}} = 2.674$ ). Reported parameters are the MCMC median values and their offsets from the 15.8 and 84.1 percentiles. Some velocities have zero uncertainties because they are fixed to those of the low-ion metal lines.

alone do not constrain their velocities well. Specifically, these components are at  $-470$  and  $-225 \text{ km s}^{-1}$  toward QSO1 and at  $-209 \text{ km s}^{-1}$  toward QSO2. The optimized models are plotted against the data as blue curves in Figure 5 and the formal parameters and their statistical uncertainties are tabulated in Table 4.

Because of the empirical nature of our placement of the unabsorbed QSO continuum, the Voigt parameters suffer from significant systematic uncertainties. In particular, we are interested in the systematic uncertainties of  $\log N_{\text{HI}}$ , which depends on (1) the column density due to the varying gradient of the curve of growth, (2) the quality of the spectrum, and (3) the significance of line blending. To quantify this, we run the same modeling procedure as above but vary the QSO continuum model by  $\pm 10\%$  and use the resulting offsets between the three formal solutions to estimate systematic uncertainties. All subsequent errors in  $\log N_{\text{HI}}$  and metallicities ( $[X/H]$ ) include both statistical and systematic uncertainties.

Figure 5 reveals that there are three separate kinematic clumps centered around  $\delta v \approx -300, +400, +1200 \text{ km s}^{-1}$  relative to  $z_{\text{SMG}} = 2.674$  (i.e.,  $z_{\text{abs}} \approx 2.6703, 2.6789, 2.6887$ ), which we designate as subsystems A, B, and C, respectively, following the nomenclature of Finley et al. (2014). The same clumps appear toward both QSOs, although their column densities vary between sightlines. Half of the six subsystems are optically thick (i.e.,  $\log N_{\text{HI}} > 17.2$ ), including two sub-DLAs (QSO1-A and QSO1-C) and one LLS (QSO2-A). Metal absorption lines from these subsystems are thus expected, as we will show in the next subsection.

### 4.3. Ionic Column Densities from the AODM Method

Figure 6 compares the velocity profiles of H I Ly $\beta$  and a selection of metal line transitions commonly observed in LLSs and DLAs (see Table 5 for transition data). We find that five of the six H I subsystems are detected in at least one metal transition; the only exception is QSO1-B. Similar to their H I absorption, the metal-line absorptions of subsystems QSO1-A and C, the two sub-DLAs, are resolved into multiple components. Note that the X-shooter spectrum has higher resolution for metal lines in the range  $1500 \text{ \AA} < \lambda_{\text{rest}} < 2700 \text{ \AA}$  ( $R = 11,000$  or  $\text{FWHM} = 27 \text{ km s}^{-1}$ ) than for the H I Lyman lines at  $\lambda_{\text{rest}} < 1217 \text{ \AA}$  ( $R = 6400$  or  $\text{FWHM} = 47 \text{ km s}^{-1}$ ). For

**Table 5**  
Selected Metal Transitions

Ion	$\lambda_{\text{rest}}$ ( $\text{\AA}$ )	$\log f$	IP <sub>0</sub> (eV)	IP <sub>1</sub> (eV)
C II	1334.5323	-0.8935	11.26	24.38
C IV	1548.2040	-0.7215	47.89	64.49
...	1550.7776	-1.0234	...	...
O I	1302.1685	-1.3188	0.00	13.62
Mg II	2796.3543	-0.2108	7.65	15.04
...	2803.5315	-0.5146	...	...
Al II	1670.7886	0.2405	5.99	18.83
Al III	1854.7183	-0.2526	18.83	28.45
Si II	1304.3702	-1.0640	8.15	16.35
...	1526.7070	-0.8761	...	...
Si IV	1393.7602	-0.2899	33.49	45.14
...	1402.7729	-0.5952	...	...
Fe II	1608.4508	-1.2388	7.90	16.20
...	2382.7642	-0.4949	...	...
...	2600.1725	-0.6209	...	...

**Note.** The columns  $\lambda_{\text{rest}}$  and  $\log f$  list the rest-frame wavelengths and the oscillator strengths (Morton 2003). The columns IP<sub>0</sub> and IP<sub>1</sub> list the ionization potentials (IPs) to create the ion from the immediate lower state and to ionize it to the immediate higher state, respectively.

each distinct metal-line cloud, we define a velocity integration window (highlighted in Figure 6) and name it by adding a number suffix to designate its associated subsystem. The cloud QSO1-C1 shows the strongest metal absorption with at least four blended components within  $\sim 200 \text{ km s}^{-1}$ . We treat it as a single entity here, because for the purpose of measuring the gas metallicity it is unnecessary to deblend these components with Voigt profile fitting. Because the absorption toward QSO2 spans a narrower velocity range than that toward QSO1, the former is missing the most blueshifted cloud “A1” and the most redshifted cloud “C2”. For completeness, we defined QSO1-B1 based on its H I absorption because no metal lines are detected there. As a result, there are a total of eight metal-line clouds. The top section of Table 6 lists the velocity integration windows of the clouds and their H I column densities by summing  $\log N_{\text{HI}}$  of the Voigt components within the velocity windows. Each cloud contains only one H I Voigt component

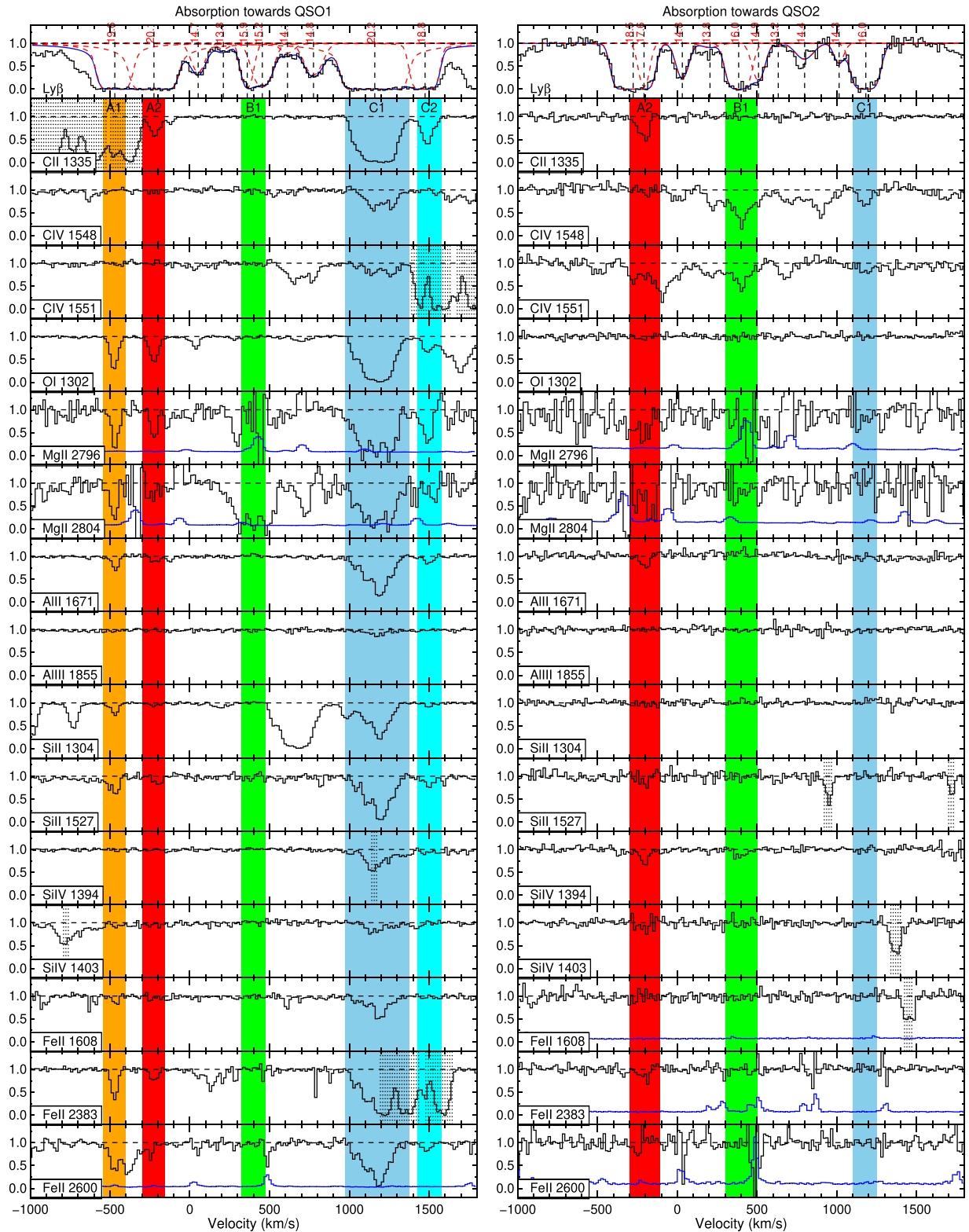


**Figure 6.** Velocity profiles of H I Ly $\beta$  and selected metal lines toward QSO1 (left) and QSO2 (right). All velocities are relative to  $z_{\text{SMG}} = 2.674$ . The velocity integration ranges of the clouds defined in Table 6 are highlighted in color. Vertical dotted lines strike out regions that are blended with lines from absorbers at other redshifts (see Appendix C). The error spectrum is plotted (blue) when it shows significant structures.

except QSO1-B1 and QSO2-A2, both of which contain two closely separated components.

In Appendix D, we provide an overview of the AODM method and our measurements of ionic column densities from all of the selected transitions (Table D1). The listed

uncertainties of the unsaturated and unblended detections in the table include both statistical and systematic errors. Column densities from the AODM method are taken as lower limits for lines with more than one saturated pixel (which we define as  $I_{\text{obs}}/I_0 \leq 0.05$  or  $\tau \geq 3$ ) and are taken as upper limits for lines

**Table 6**  
Properties of Metal-line-defined Clouds

Quantity	QSO1-A1	QSO1-A2	QSO1-B1	QSO1-C1	QSO1-C2	QSO2-A2	QSO2-B1	QSO2-C1
$\delta v/\text{km s}^{-1}$	[−545, −405]	[−295, −155]	[325, 475]	[975, 1375]	[1425, 1575]	[−300, −110]	[300, 500]	[1100, 1250]
$\log N_{\text{HI}}$	$19.64^{+0.04}_{-0.06}$	$20.06^{+0.08}_{-0.05}$	$15.98^{+0.39}_{-0.23}$	$20.23^{+0.07}_{-0.08}$	$18.79^{+0.33}_{-0.25}$	$18.59^{+0.23}_{-0.43}$	$16.03^{+0.21}_{-0.16}$	$16.00^{+0.10}_{-0.09}$
$\log(\text{C IV}/\text{C II})$	...	<−1.06	...	<−1.10	<−1.23	<−0.80	>0.93	>0.36
$\log(\text{Al III}/\text{Al II})$	<−0.20	<0.17	...	−0.58	<0.00	<0.22	...	...
$\log(\text{Si IV}/\text{Si II})$	<−1.47	<−0.92	...	−1.22	<−0.86	>−0.37	...	...
$\log U$	<−3.4	<−2.9	...	−3.0	<−3.2	−2.9	>−2.1	>−2.5
$\log U$ , adopted	−3.5	−3.0	−2.0	−3.0	−3.5	−3.0	−2.0	−2.0
$\log(n_{\text{H}}/\text{cm}^{-3})$	−1.4	−1.9	−2.9	−1.9	−1.4	−1.9	−2.9	−2.9
$\log(N_{\text{H}}/\text{cm}^{-2})$	19.9	20.4	19.5	20.5	19.7	20.1	19.5	19.5
$\log f_{\text{HI}}$	−0.3	−0.3	−3.5	−0.3	−0.9	−1.5	−3.5	−3.5
$\log(l/\text{pc})$	2.8	3.9	3.9	3.9	2.6	3.5	3.9	3.9
$[\alpha/\text{H}]$	$−1.77 \pm 0.06$	$−2.28 \pm 0.08$	...	$−1.08 \pm 0.08$	$−1.15 \pm 0.30$	$−1.91 \pm 0.34$	$−1.02 \pm 0.19$	$−1.58 \pm 0.15$
Ion	O I	O I	...	Si II	O I	C II	C IV	C IV
IC	−0.01	−0.01	...	−0.12	−0.04	−0.90	−2.82	−2.82
$[\text{Fe}/\text{H}]$	$−1.92 \pm 0.07$	$−2.62 \pm 0.14$	...	$−1.27 \pm 0.09$	$−1.76 \pm 0.34$	...	...	...
$[\alpha/\text{Fe}]$	$+0.15 \pm 0.09$	$+0.34 \pm 0.16$	...	$+0.19 \pm 0.12$	$+0.61 \pm 0.45$	...	...	...

**Note.** The first section gives the AODM velocity integration windows (relative to  $z_{\text{sys}} = 2.674$ ) and the total H I column densities of the Voigt components within these windows (the errors include systematic uncertainties due to continuum placement). The second section lists the observed ionic column density ratios, and their joint constraints on the ionization parameter ( $\log U$ ). The third section lists the quantities implied by the CLOUDY model for the adopted  $\log U$  and  $\log N_{\text{HI}}$ : total H volume density ( $\log n_{\text{H}}$ ), total H column density ( $\log N_{\text{H}}$ ), neutral H fraction ( $\log f_{\text{HI}}$ ), and characteristic line-of-sight depth ( $\log l$ ). The last section lists the adopted  $\alpha$ -element metallicity ( $[\alpha/\text{H}]$ ), the preferred ion, the ionization correction, the iron metallicity ( $[\text{Fe}/\text{H}]$ ), and the  $\alpha$ -enhancement relative to iron ( $[\alpha/\text{Fe}]$ ).

that are blended with transitions from absorbers at other redshifts. Lastly, for undetected transitions, we quote  $3\sigma_{\text{sta}}$  upper limits on the column densities. Systematic errors are not used here because it is not meaningful to adjust the QSO continuum around an undetected transition.

#### 4.4. Ionization Correction and Metallicities

A relative metallicity measurement of the intervening gas requires (1) H I column density, (2) ionic column density of a metal element, (3) the reference solar abundances, and (4) the ionization correction. The definition of the relative metallicity makes this explicit:

$$\begin{aligned}
 [\text{X}/\text{H}] &\equiv \log(N_{\text{X}}/N_{\text{H}}) - \log(N_{\text{X}}/N_{\text{H}})_{\odot} \\
 &= [\log(N_{\text{X}_i}/N_{\text{HI}}) - \log(N_{\text{X}}/N_{\text{H}})_{\odot}] \\
 &\quad + (\log f_{\text{HI}} - \log f_{\text{X}_i}) \\
 &\equiv [\text{X}/\text{H}]' + \text{IC}
 \end{aligned} \tag{6}$$

where  $\text{X}_i$  denotes the ionic state  $i$  of element X,  $f_{\text{X}_i} \equiv N_{\text{X}_i}/N_{\text{X}}$  is the fraction of the element in the ionic state  $i$ ,  $f_{\text{HI}} \equiv N_{\text{HI}}/N_{\text{H}}$  is the neutral fraction of hydrogen,  $[\text{X}/\text{H}]' \equiv \log(N_{\text{X}_i}/N_{\text{HI}}) - \log(N_{\text{X}}/N_{\text{H}})_{\odot}$  is the raw metallicity, and  $\text{IC} \equiv \log f_{\text{HI}} - \log f_{\text{X}_i}$  is the ionization correction.

We have obtained the first two items ( $\log N_{\text{HI}}$  and  $\log N_{\text{X}_i}$ ) in Sections 4.2 and 4.3 and the results are listed in Tables 4 and D1. Combined with the elemental abundances of the present-day solar photosphere from Asplund et al. (2009), we are ready to calculate the raw metallicity  $[\text{X}/\text{H}]'$ . Next, we calculate the ionization correction (IC) using CLOUDY photoionization models (Ferland et al. 2017).

The IC factors are sensitive to both the H I column density ( $\log N_{\text{HI}}$ ) and the ionization parameter  $\log U = \log(\Phi_{\text{H}}/n_{\text{H}}c)$ , where  $\Phi_{\text{H}}$  is the surface flux of ionizing photons with  $h\nu > 1$

Ryd at the illuminated face. The former has been measured, but the latter needs to be constrained by comparing the column density ratios of different ionic states of the same elements and predictions from photoionization models. Therefore, for each cloud listed in Table 6, we calculate a set of photoionization models, with a termination condition set to meet the observed H I column density. For the ionizing source, we use the radiation background of Haardt & Madau (2012) interpolated to  $z = 2.67$  with contributions from both galaxies and quasars. For the cloud, we assume plane-parallel geometry, the solar relative abundance pattern, a metallicity of  $[\text{M}/\text{H}] = -1.5$ ,<sup>16</sup> and a range of hydrogen volume densities ( $1.09 \geq \log(n_{\text{H}}/\text{cm}^{-3}) \geq -4.91$ ) to cover ionization parameters in the range  $-6 \leq \log U \leq 0$ . For each cloud, we compare the observed ionic column ratios (C IV/C II and Si IV/Si II) and the model-predicted ratios to constrain the ionization parameter. We list the constraints on  $\log U$  in Table 6. It is rare to have detections of both high ions and low ions in the same cloud, leading to many upper or lower limits on  $\log U$ . But we found that the most plausible ionization parameters lie in the range  $-4 \lesssim \log U \lesssim -2$ , comparable to other published LLSs (e.g., Prochaska 1999; Lehner et al. 2016). Depending on the data constraint, we adopt  $\log U$  values of  $-3.5$ ,  $-3.0$ , or  $-2.0$  for each cloud. Finally, once both  $\log N_{\text{HI}}$  and  $\log U$  are fixed, we use the CLOUDY model of the same parameters to calculate the ICs for all of the ions (Table D2), which are then used to obtain the ionization-corrected metallicity measurements for all of the transitions (Table D3). Notice that the ionization correction only becomes important for (1) low ions in clouds with  $\log N_{\text{HI}} \lesssim 19$  and (2) intermediate or high ions (e.g., C IV and Si IV) at all column densities. For low ions in sub-DLAs, the ICs are fairly small ( $\pm 0.15$  dex). We also use the model to

<sup>16</sup> The derived ICs are insensitive to the assumed metallicity.

infer the total H column density ( $\log N_{\text{H}}$ ), the H neutral fraction ( $\log f_{\text{H I}}$ ), the H volume density ( $\log n_{\text{H}}$ ), and the characteristic line-of-sight depth of the cloud ( $\log l = \log N_{\text{H}} - \log n_{\text{H}}$ ). The results are listed in Table 6.

The best metallicity measurement is provided by O I, because O I has the smallest ionization correction factors due to its charge-exchange reactions with hydrogen (Field & Steigman 1971) and its hydrogen-like ionization potential. Unfortunately, O I  $\lambda 1302$  is saturated in C1 toward QSO1 (a common issue of the transition for DLAs) and is undetected in cloud B toward QSO1 and the clouds toward QSO2. As a result, transitions from other ions need to be used. The bottom section of Table 6 lists the final adopted metallicities from our preferred  $\alpha$ -element transitions and Fe II. Note that the ICs for QSO2-B1 and QSO2-C1 are large because only the C IV lines are detected in these clouds. We fail to obtain a reliable metallicity measurement for QSO1-B1 because of the absence of metal absorption. For the four clouds where we have both  $[\alpha/\text{H}]$  and  $[\text{Fe}/\text{H}]$ , we found a moderate level of  $\alpha$ -enhancement ( $[\alpha/\text{Fe}]$ ) between 0.15 and 0.61 (with an inverse-variance-weighted mean of 0.2), comparable to those previously measured in  $z > 2$  DLAs ( $[\alpha/\text{Fe}] = 0.30 \pm 0.16$ ; Rafelski et al. 2012).

We opt not to correct the gas-phase metallicity for dust depletion, because (1) little depletion is expected from volatile elements such as O and C, (2) the SDSS spectra and photometry of the QSOs show no evidence of significant dust reddening, and (3) the depletion factors are largely uncertain in external galaxies. As a reference, in the Milky Way’s ISM, volatile elements (e.g., C, N, O, S, Zn) show depletions of  $(X/\text{H})_{\text{ISM}} - (X/\text{H})_{\text{gas}} \lesssim 0.3$ , while refractory elements (e.g., Mg, Al, Si, Fe, Ni) show  $0.7 \lesssim (X/\text{H})_{\text{ISM}} - (X/\text{H})_{\text{gas}} \lesssim 2.0$  (Savage & Sembach 1996; Groves et al. 2004). These local measurements from a metal-rich ISM provide strict upper limits on the level of depletion expected in the CGM of the SMG.

## 5. Emission–Absorption Connection

Identifying the emission counterparts of the intervening gas helps us to compare the properties of the galaxies to those of their CGM. Having analyzed the ALMA CO emitters in Section 3 and the QSO absorption spectra in Section 4, we are now ready to draw connections between the emission and the absorption based on proximity in both spatial and redshift dimensions.

Figure 7 directly compares the absorption profiles from the QSOs to the CO emission profiles from the SMG and its companions. The H I Ly $\beta$  and Al II  $\lambda 1670.8$  profiles from the two QSOs are plotted together to illustrate the striking kinematic coherence. In addition, the figure illustrates  $\log N_{\text{H I}}$  from the Voigt profile solution in Table 4 and the ionization-corrected metallicities of the metal-line-defined clouds in Table 6.

In Section 4, we have found that the  $z_{\text{abs}} \approx 2.68$  H I absorbers have total H I column densities of  $\log N_{\text{H I}} = 20.53^{+0.06}_{-0.06}$  and  $18.60^{+0.23}_{-0.43}$  toward QSO1 and QSO2, respectively. Each absorber is resolved into three main subsystems (A, B, and C) with velocity spans of  $\sim 1500$ – $2000 \text{ km s}^{-1}$ . Although their H I column densities vary significantly between the two QSO sightlines, their radial velocities show remarkable consistency, indicating that the QSOs are intercepting three expansive sheets/filaments of gas. At the same time, the extreme velocity

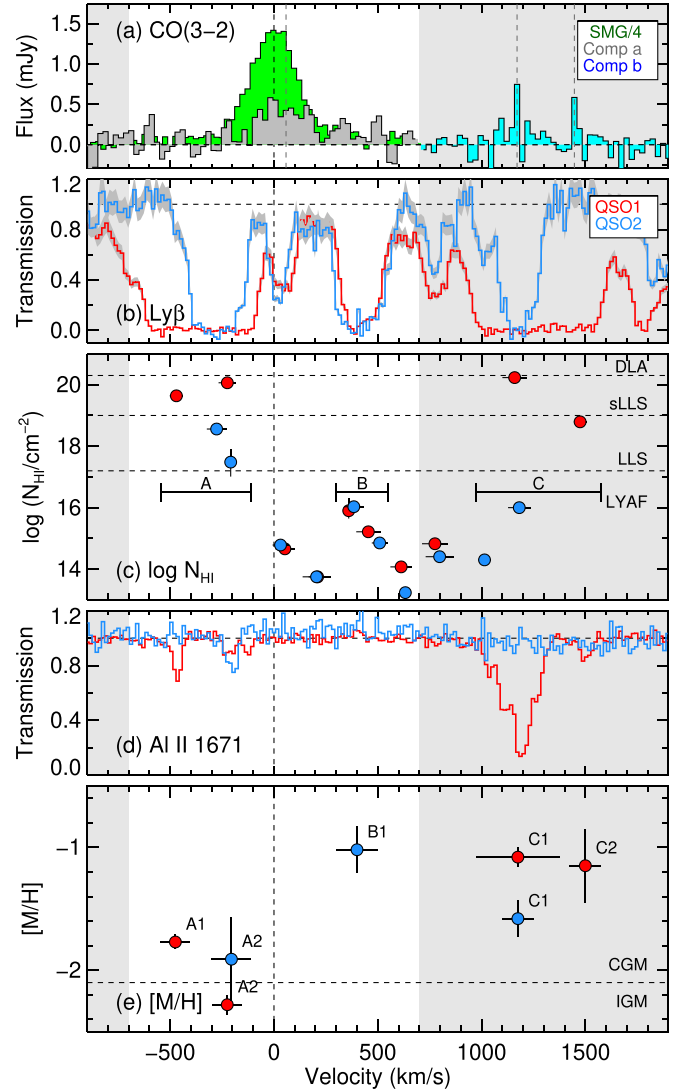


**Figure 7.** Comparison of emission and absorption. (a) CO(3–2) spectra of the SMG and its companions, (b) H I Ly $\beta$  absorption, (c) H I column densities of Voigt components (Table 4), (d) Al II  $\lambda 1670.8$  absorption, and (e) metallicities of metal-line-defined clouds (Table 6). The absorbers toward QSO1 and QSO2 are color-coded in red and blue, respectively. In (a), the SMG spectrum has been divided by 4 to show it together with the spectra of its companions, and the vertical dashed lines indicate the centroid velocities of the CO emission lines at 0, 58, 1171, and 1447 km s $^{-1}$ . All velocities are relative to the redshift of the SMG ( $z_{\text{SMG}} = 2.674$ ), and the gray shaded regions indicate velocities beyond the escape velocity of a  $10^{13} M_{\odot}$  halo ( $v_{\text{esc}} \simeq 700 \text{ km s}^{-1}$ ).

widths of the absorption-line systems suggest that they probe merging systems (Prochaska et al. 2019).

Results in Figure 7 show that subsystem C is unlikely to be in the same halo as subsystems A, for several reasons. First, subsystem C is  $10\times$  more metal-enriched than subsystem A ( $[\text{M}/\text{H}] \simeq -1.1$  versus  $-2.1$ ). Second, the velocity spans of  $\sim 1950 \text{ km s}^{-1}$  (QSO1) and  $\sim 1460 \text{ km s}^{-1}$  (QSO2; Table 4) and their asymmetric distributions around  $z_{\text{SMG}}$  (absorption is centered at  $z_{\text{abs}} = 2.68$ ) are inconsistent with gravitational motions inside even a  $10^{13} M_{\odot}$  halo centered on the SMG, because the escape velocity of such a halo following the NFW profile is flat at  $\sim 700 \text{ km s}^{-1}$  between 60 kpc and the virial radius of 186 kpc. Lastly, we have detected CO emission at almost exactly the redshifts of the absorbing clouds in subsystem C in Comp b, which lies much closer to the QSOs

**Table 7**  
Properties of the CGM around the SMG and Comp b

Name	$\delta v$ (km s <sup>-1</sup> )	Galaxy	$R_{\perp}$ (kpc)	$\log(N_{\text{HI}}/\text{cm}^{-2})$	[M/H]
QSO1-A	[-545, -110]	SMG	93.1	20.20 <sup>+0.07</sup> <sub>-0.05</sub>	-2.09 ± 0.07
QSO2-A	...	...	175.5	18.59 <sup>+0.23</sup> <sub>-0.43</sub>	-1.91 ± 0.34
QSO1-B	[300, 550]	SMG	93.1	15.98 <sup>+0.39</sup> <sub>-0.23</sub>	...
QSO2-B	...	...	175.5	16.06 <sup>+0.20</sup> <sub>-0.15</sub>	-1.02 ± 0.19
QSO1-C	[975, 1575]	Comp b	58.9	20.25 <sup>+0.06</sup> <sub>-0.07</sub>	-1.09 ± 0.11
QSO2-C	...	...	32.2	16.01 <sup>+0.10</sup> <sub>-0.09</sub>	-1.58 ± 0.15

than the SMG. Therefore, we consider subsystem A to be part of the CGM of the SMG at  $z = 2.674$ , and subsystem C part of the CGM of Comp b at  $z = 2.6884$  and  $2.6917$ .

As for subsystem B ( $\log N_{\text{HI}} \simeq 16$ ), although its velocity allows an association with the SMG, it is unimportant because its contribution to the CGM is negligible compared to subsystem A.

Once the emission counterparts are determined, the absorption-line measurements from the two QSO sightlines can be plotted against the impact parameter to show crude radial profiles of the CGM around the SMG and Comp b. We consolidate the results in Table 7, where we have assigned a velocity window for each subsystem that captures its major clouds. We calculate the total HI column densities from the HI Voigt components within these velocity windows. When there are multiple metal-line clouds in a subsystem, the metallicity is calculated as the  $N_{\text{H}}$ -weighted mean  $[\alpha/\text{H}]$ , where  $N_{\text{H}}$  is the HI + H II column density based on the adopted CLOUDY model.

The GAMA J0913–0107 system gives us the first glimpse into the CGM around an SMG. With high HI column density and low metallicity at large impact parameters, the CGM of the SMG is distinct from the CGM of QSOs and normal star-forming galaxies at  $z \sim 2-3$ .

The profile of HI column density is shown in Figure 8(a). We compare our measurements with literature QSO absorption-line measurements in the surroundings of  $z \sim 2-3$  QSOs (Lau et al. 2016) and LBGs (Simcoe et al. 2006; Rudie et al. 2012; Crighton et al. 2013, 2015). The HI column densities of the SMG’s CGM, similar to coeval QSOs, are significantly greater than those of star-forming galaxies at  $R_{\perp} \gtrsim 70$  kpc. The HI column density declines as we move away from the SMG, with a gradient of  $-2.0 \pm 0.4$  dex per 100 kpc. How do the observed column densities compare with the projected surface mass density  $\Sigma_{\text{M}}(R)$  of NFW halos? To make this comparison, we first calculate  $\Sigma_{\text{M}}(R)$  by integrating the NFW density profile  $\rho(r)$  up to the virial radius:

$$\Sigma_{\text{M}}(R) = 2 \int_R^{R_{\text{vir}}} \frac{r\rho(r)}{\sqrt{r^2 - R^2}} dr. \quad (7)$$

We then convert it to HI column densities by assuming a baryon–dark-matter density ratio of  $f_b \equiv \Omega_b/\Omega_c = 0.187$  (Planck Collaboration et al. 2020), a helium correction of  $f_{\text{He}} = M_{\text{H+He}}/M_{\text{H}} = 1.36$ , and an arbitrary neutral fraction of 10%.<sup>17</sup> Figure 8(a) shows that the HI column density profiles of the SMG and the QSOs are consistent with the expectation from a  $\sim 10^{13} M_{\odot}$  halo. This is in agreement with the detection

of a high column of HI ( $\log N_{\text{HI}} = 18.6$ ) at an impact parameter as far as 176 kpc. The agreement also shows that the neutral gas in the absorption-line systems can account for  $\sim 10\%$  of the total baryonic mass in the halo if they have a filling factor close to unity. On the other hand, the  $\log N_{\text{HI}}$  profile of LBGs is more consistent with a  $\sim 10^{12} M_{\odot}$  halo.

The metallicity profile is shown in Figure 8(b). The literature data points show that metal-enriched gas with  $-1 \lesssim [\text{M}/\text{H}] \lesssim 0$  dominates the inner part ( $R_{\perp} \lesssim 150$  kpc) of the CGM around both QSOs and LBGs. By contrast, the CGM of the SMG is poor in metal, with an almost constant metallicity of  $[\text{M}/\text{H}] \approx -2$  across two sightlines separated by 86 kpc ( $10''8$ ). Its metallicity is near the  $1\sigma$  upper bound of the metallicities measured in the LYAF (i.e., the IGM; Simcoe et al. 2004), and it is lower by  $\sim 1.5$  dex at  $R_{\perp} = 93.1$  and by  $\sim 0.5$  dex at  $R_{\perp} = 175.5$  kpc than that of the CGM of QSOs.

On the other hand, the CGM of Comp b shows properties similar to that of normal star-forming galaxies at  $z \sim 2-3$ . Both line emitters in Comp b have orders-of-magnitude lower molecular gas mass than the SMG (see Table 1). Assuming a correction factor from CO to molecular mass of  $\alpha_{\text{CO}} = 4.3$  and a CO excitation correction of  $r_{31} = 0.52$ , the emitters at  $z = 2.6884$  and  $2.6917$  have molecular gas masses of  $M_{\text{mol}} = 5.6 \times 10^9$  and  $4.4 \times 10^9 M_{\odot}$ , respectively. The gas masses are comparable to those measured in the lensed normal star-forming galaxies that have stellar masses of  $\sim 10^{10} M_{\odot}$  (Saintonge et al. 2013). One would thus expect a CGM similar to that of LBGs. The corresponding subsystem C provides absorption-line measurements at  $R_{\perp} = 32.3$  and  $58.9$  kpc. It shows significantly metal-enriched gas (compared to the IGM level) with a large variation in HI column density over a difference of just 27 kpc in impact parameter. Comp b is thus surrounded by a metal-enriched clumpy medium that extends to at least  $\sim 60$  kpc.

In the above, we have shown that the CGM of SMM J0913 is distinctly different from the CGM of QSOs and normal star-forming galaxies. But how do our absorbers compare with other DLAs in terms of absorption-line properties only? The HI column densities of subsystems A and C toward QSO1 miss the DLA threshold of  $\log N_{\text{HI}} = 20.3$  by merely  $\sim 0.1$  dex. Because such small differences are comparable to the measurement uncertainty, more liberal thresholds have been used to select DLAs (e.g.,  $\log N_{\text{HI}} > 20.1$  in Rubin et al. 2015). Combined with the result that the two sub-DLAs have neutral fraction of  $\sim 50\%$  from CLOUDY models, we believe that it is appropriate to compare their properties with those of the general DLA population.

With high-resolution spectra of 100 DLAs at  $z_{\text{abs}} \sim 2-4$ , Rafelski et al. (2012) found that their metallicity distribution is well fit by a Gaussian with a mean at  $[\text{M}/\text{H}] = -1.57$  and a

<sup>17</sup> Comparable to the neutral fractions estimated by our photoionization models in Table 6.

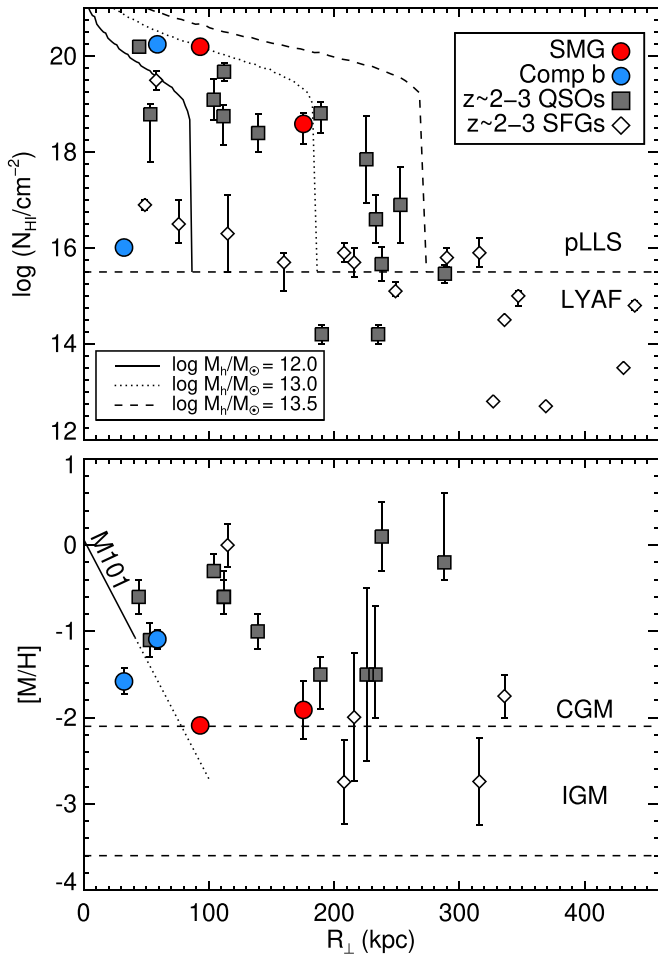


**Figure 8.** Profiles of the CGM around the SMG (red) and Comp b (blue). Top: H I column density vs. projected separation for the absorption-line clouds in GAMA J0913–0107 and the literature. The curves show the projected H I column densities of NFW halos, where the precipitous decline marks the virial radii. Bottom: metallicity vs. projected separation for the absorption-line clouds in GAMA J0913–0107 and the literature. Literature QSO CGM data are from Lau et al. (2016), SFG  $\log N_{\text{HI}}$  data are from Simcoe et al. (2006), Rudie et al. (2012), and Crighton et al. (2013, 2015), and SFG  $[M/H]$  data are from Simcoe et al. (2006). The horizontal dashed lines in the bottom panel indicate the range of IGM metallicities measured from the LYAF at  $z_{\text{abs}} \sim 2.5$  ( $[M/H] = -2.85 \pm 0.75$ ; Simcoe et al. 2004). The sloping line shows the oxygen abundance profile of the giant spiral galaxy M101 measured with an electron-temperature-based method (Equation (5) of Kennicutt et al. 2003). The solid portion is covered by H II regions, while the dotted portion is an extrapolation.

dispersion of 0.57 dex. The DLA metallicity only mildly decreases with redshift, but shows a strong correlation with the width of low-ion metal lines (e.g.,  $\Delta V_{90}$  or  $W_{1526}$ ) (Neeleman et al. 2013). This correlation between kinematics and metallicity is generally interpreted as a manifestation of the mass–metallicity relation (e.g., Tremonti et al. 2004; Erb et al. 2006), because the line width may reflect the halo mass (like in the Tully–Fisher relation), which in turn is proportional to the stellar mass (Møller et al. 2013).

Previous works have used higher-resolution spectra ( $R \gtrsim 40,000$ ) to measure  $\Delta V_{90}$ , the velocity interval including 90% of the optical depth of an *unsaturated* line. And the alternative kinematic parameter  $W_{1526}$ , the rest-frame equivalent width of Si II  $\lambda 1526.7$ , is unsuitable for our sub-DLAs because the line is *unsaturated* (see Figure 6). The equivalent width only becomes a good kinematics indicator when the line is *saturated*, weakening its dependence on the Si<sup>+</sup> column

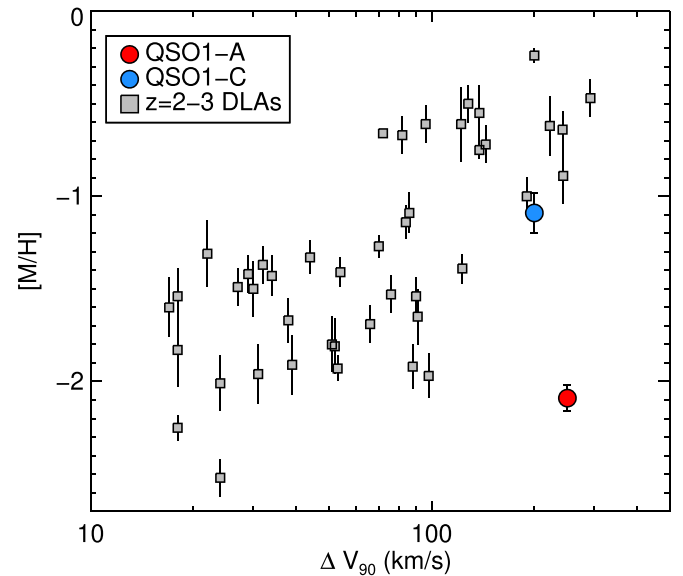


**Figure 9.** Metallicity–line width relation of (sub-)DLAs at  $z \sim 2$ –3. Gray squares are 44 DLAs in the range  $2 < z_{\text{abs}} < 3$  compiled from the literature (Neeleman et al. 2013). The red and blue circles show respectively subsystems A and C toward QSO1. For both sub-DLAs, we have estimated the velocity widths using the separation of resolved components in the  $R \sim 11,000$  X-shooter/VIS spectrum.

density (and consequently on metallicity). So to place our sub-DLAs on the relation, we adopt the velocity separation between kinematically resolved substructures as a surrogate of  $\Delta V_{90}$ . QSO1-A shows two velocity components of similar strength separated by  $\sim 250 \text{ km s}^{-1}$ , and QSO1-C is dominated by the stronger C1 cloud, which appears to be a blend of four components with a velocity span of  $\sim 200 \text{ km s}^{-1}$ . These estimates of the velocity width should be considered as lower limits on  $\Delta V_{90}$ , because they are the separations between peak optical depths.

Figure 9 compares the two sub-DLAs against literature DLAs. To control the redshift evolution of the mass–metallicity relation, only the DLAs in the range  $2 < z_{\text{abs}} < 3$  are plotted. While QSO1-C blends into the general trend established by DLAs, QSO1-A is a clear outlier. First, very few DLAs have metallicities as low as QSO1-A: only two out of the 44 DLAs ( $4.5^{+5.5}_{-1.5}\%$ ) have  $[M/H] \leq -2.1$ . Second, its high velocity width places it significantly below the metallicity–line width relation of DLAs, which would have predicted a velocity width of only  $\sim 20 \text{ km s}^{-1}$  based on its metallicity at  $[M/H] = -2.1$ .

This finding suggests that most of the DLAs are likely closer to their hosts than our sub-DLA QSO1-A ( $R_{\perp} = 93 \text{ kpc}$ ), consistent with previous observations of DLA host galaxies (see Section 1.3). More importantly, the unusual combination of high velocity width and low metallicity provides a method—based on absorption-line properties alone—to potentially separate (sub-)DLAs associated with normal star-forming galaxies at small impact parameters from those associated with more massive galaxies such as SMGs at large impact parameters.

## 6. Summary and Discussion

We have carried out a comprehensive study of the emission–absorption system GAMA J0913–0107 at  $z \sim 2.67$  with a multiwavelength data set obtained primarily from Herschel, ALMA, and VLT/X-shooter. The system consists of a bright

SMG, its CO companion galaxies, and a number of optically thick HI absorbers toward two background QSOs within  $22''$  of the SMG. Our main results are:

1. The Herschel-selected SMG at  $z = 2.674$ , with an  $870 \mu\text{m}$  flux of  $7.4 \text{ mJy}$  and an IR luminosity of  $\sim 10^{13} L_{\odot}$ , is one of the most luminous dusty star-forming galaxies. Its properties are similar to the general SMG population at  $z \sim 2$ , featuring a short gas depletion timescale of  $\sim 0.1 \text{ Gyr}$  and compact (subarcsecond) sizes in both dust emission and CO(3–2) emission. The high-S/N spectrum reveals two CO(3–2) components at almost the same redshift:  $\sim 1/4$  of the line flux is in a broad component with  $\text{FWHM} \simeq 900 \text{ km s}^{-1}$ , while  $\sim 3/4$  of the flux is in a narrow component with  $\text{FWHM} \simeq 250 \text{ km s}^{-1}$ .
2. Three companion CO emitters are identified within  $30''$  and  $1500 \text{ km s}^{-1}$  of the SMG. A comparison with the source counts from the ASPECS field survey indicates that the SMG lives in an overdense environment.
3. Two nearby QSOs provide background beacons to probe the CGM of the SMG. A DLA with a total HI column density of  $\log N_{\text{HI}} = 20.5$  is identified at  $z_{\text{abs}} \sim 2.68$  in the closer QSO sightline at  $\theta = 11''.7$ . The DLA is quite unusual, in terms of both the large impact parameter ( $R_{\perp} = 93.1 \text{ kpc}$  to the SMG) and the enormous velocity span ( $\sim 2000 \text{ km s}^{-1}$ ). X-shooter resolved the DLA into three major subsystems, including two sub-DLAs with distinctly different metallicities separated by  $\sim 1600 \text{ km s}^{-1}$ . Remarkably, the same subsystems are also found in the farther QSO sightline at  $\theta = 22''.1$ : they have nearly the same velocities and metallicities as their counterparts at  $\theta = 11''.7$ , despite lower HI column densities (total  $\log N_{\text{HI}} = 18.6$ ).
4. We use the absorption-line systems to characterize the CGM of the SMG and its companion Comp b, and we compare their properties with the CGM of QSOs and normal star-forming galaxies. The CGM of the SMG forms its own category: while its high column densities at large impact parameters are similar to the massive halos inhabited by  $z = 2\text{--}3$  QSOs, its metal content ( $\sim 1\%$  solar) is an order of magnitude lower than the circum-QSO medium. On the other hand, the CGM of the much less luminous Comp b is more consistent with that of normal star-forming galaxies at  $z = 2\text{--}3$ , showing significant metal enrichment ( $\sim 10\%$  solar) within  $R_{\perp} \lesssim 60 \text{ kpc}$ .

The detection of a high column density of mostly neutral, metal-poor gas in the CGM of a massive dusty starburst galaxy at  $z = 2.674$  has powerful implications for theories of galaxy formation and evolution. The remarkable consistency of the HI absorbers in both kinematics and metallicity across two sightlines separated by  $86 \text{ kpc}$  is at odds with CGM models that assume randomly floating HI clouds in pressure equilibrium with hot X-ray gas. Instead, it is logical to assume that the background QSOs have intercepted a single filament of cool gas permeating the halo.

Narrow filaments of cool gas and satellite galaxies can penetrate the hot CGM of massive halos without ever being shock-heated to the virial temperature, because (1) massive halos are rare and tend to form at the intersections of the cosmic web and (2) the cooling time is shorter in the filaments than in

the halo (Dekel & Birnboim 2006; Dekel et al. 2009; Kereš et al. 2009). At  $z \gtrsim 2.5$ , such cold streams can survive even in halos more massive than  $\sim 10^{13} M_{\odot}$  (although note that this mass limit is highly uncertain). In particular, stream-feeding is likely important in the bright SMGs with  $S_{850} > 5 \text{ mJy}$  because their comoving space density exceeds the expectation from minor and major mergers (Dekel et al. 2009).

The observed properties of the absorption-line systems match the simulation-predicted properties of cold streams. First, the simulations of Dekel et al. (2009) show that the inflow velocity is comparable to the virial velocity and is roughly constant along the filament. This is consistent with the velocity shift ( $\delta v = -300 \text{ km s}^{-1}$ ) and the kinematic coherence we saw between the clouds in both QSO sightlines. Second, by post-processing gas in seven simulated halos with  $M_{\text{halo}} = 10^{10}\text{--}10^{12} M_{\odot}$  in the range  $1.5 < z < 4.0$ , Fumagalli et al. (2011) found that the absorption-line systems associated with the smooth stream component have systematically lower metallicity ( $\sim 1\%$  solar). This is exactly the level of the gas metallicity we measured in the absorbers associated with the SMG.

Radially inflowing on nearly a freefall timescale, the cold streams may account for the bulk of the baryonic accretion rate and become the dominant mechanism to feed the growth of galaxies (Kereš et al. 2009). We can crudely estimate the gas accretion rate from the filament that the QSOs intercepted. The filament has a length  $> 176 \text{ kpc}$  and a depth of the order of  $10 \text{ kpc}$  at  $R_{\perp} = 93 \text{ kpc}$ . The former is estimated from the impact parameter of QSO2, and the latter from the ratio between the column density and the volume density of hydrogen,  $l = N_{\text{H}}/n_{\text{H}}$ , inferred from the photoionization model of the sub-DLA QSO1-A2. The ratio of depth to distance is  $0.11 \text{ radian}$  or  $6^{\circ}$ , comparable to the opening angles of  $20\text{--}30^{\circ}$  seen in simulations (Dekel et al. 2009). Our photoionization models also indicate similar HI + HII column densities for QSO1-A2 ( $\log N_{\text{H}} = 20.4$ ) and QSO2-A2 ( $\log N_{\text{H}} = 20.1$ ), the two main clouds associated with the SMG at  $R_{\perp} = 93$  and  $176 \text{ kpc}$ . By assuming an opening angle of  $\beta = 25^{\circ}$ , an average hydrogen column density of  $\log N_{\text{H}} = 20.2$ , and a  $10^{13} M_{\odot}$  NFW halo at  $z = 2.674$ , we estimate that the mass of the filament is  $M_{\text{fil}} = f_{\text{He}} m_{\text{p}} N_{\text{H}} (\beta R_{\text{vir}}^2 / 2) \sim 1.3 \times 10^{10} M_{\odot}$ . Given an accretion timescale of  $\tau_{\text{acc}} = R_{\text{vir}} / V_{\text{vir}} = 4 \times 10^8 \text{ yr}$ , the gas accretion rate from this single filament is  $\sim 33 M_{\odot} \text{ yr}^{-1}$ . Typically three main filaments are seen in the simulations, so our estimate shows that cold-mode accretion can supply gas at a rate of  $\sim 100 M_{\odot} \text{ yr}^{-1}$ . Although accounting for only  $\sim 10\%$  of the current SFR, our estimated cool gas accretion rate is in fact comparable to the rate of total gas supply to the central galaxies in  $10^{13} M_{\odot}$  halos at  $z = 2$  from cosmological simulations (see Figure 9 of Kereš et al. 2009), and at this rate the molecular gas reservoir of  $10^{11} M_{\odot}$  can be acquired in just  $\sim 1 \text{ Gyr}$ . On the other hand, star formation at the current intensity seems unsustainable despite the efficient gas supply from cold streams.

In this work, we have presented the first observational evidence that supports the existence of cold streams in the CGM of a massive starburst galaxy. The GAMA J0913–0107 system has an excellent data set and the results are highly informative, but larger samples are clearly desired to draw conclusions on the general properties of the CGM. We hope that this will serve as a springboard for upcoming statistical

studies of the CGM in similar galaxies. As an attempt to inform these future studies, it is worth discussing the major technical challenges we had faced in this program:

1. The large beam of Herschel ( $17''.8$  at  $250\ \mu\text{m}$ ) makes it inefficient to identify SMG–QSO pairs with small angular separations ( $\theta \lesssim 10''$ ). As a result, QSO1 in GAMA J0913–0107 is the only one that probes below 100 kpc; and despite intercepting a sub-DLA it has yet to expose the chemically enriched area of the CGM of the SMG.
2. High-S/N spectra with moderately high spectral resolution are needed to unambiguously detect optically thick absorbers with  $17.2 < \log N_{\text{HI}} \lesssim 19$ . For example, with the  $R \sim 2000$  SDSS spectrum of QSO2, we could not have identified the LLS associated with the SMG (i.e., QSO2-A2 with  $\log N_{\text{HI}} = 18.6$ ). But the LLS is unambiguously detected in the X-shooter spectrum because of its resolved H I Lyman profiles and the clear detection of low-ion metal lines. Similarly low column densities are expected in most of our sample, because all of the other spectroscopically confirmed SMG–QSO pairs we have so far have impact parameters in the range  $100\ \text{kpc} < R_{\perp} < 300\ \text{kpc}$  (Fu et al. 2016, and unpublished data) and none of them show obvious (sub-)DLA features (which may be expected given the large impact parameters).
3. It has been difficult to obtain spectroscopic redshifts of the Herschel sources because (1) they require subarcsecond positions from interferometers to place spectroscopic slits, (2) the near-IR spectral range suffers from heavy telluric absorption and OH emission, and (3) SMGs tend to be weak in rest-frame optical lines. The latter two points are the main reasons why our redshift success rate is only  $\sim 60\%$ .

Possible solutions to these issues may already be on the horizon. To address the first challenge, we need to design an efficient interferometer imaging survey, because a sample of Herschel sources with less than  $10''$  apparent offsets from optical QSOs is likely overwhelmed by contaminating sources. Two thirds of the Herschel–SDSS-selected pairs with apparent separations between  $5''$  and  $10''$  turned out to be IR-luminous QSOs instead of projected SMG–QSO pairs. A good strategy is to observe multiple sources located within a circle of  $\sim 10^\circ$  diameter in a single ALMA scheduling block (SB). In Fu et al. (2017), we managed to observe  $\sim 10$  targets in a single  $\sim 50$  minutes SB, achieving an on-source integration time of 200 s per source and an rms of  $0.12\ \text{mJy beam}^{-1}$ . Do we have enough such pairs to populate a 50 minutes SB? The surface density of Herschel–QSO pairs with offsets less than  $10''$  is  $0.16\ \text{deg}^{-2}$  (26 pairs in the  $161.6\ \text{deg}^2$  H-ATLAS GAMA fields), which gives  $\sim 13$  targets for a circle of  $\sim 10^\circ$  diameter.

To address the second challenge, we need QSO spectra with quality similar to the X-shooter spectra presented here to better sample the spatial profile of the CGM. The QSOs in our sample are selected to have  $g < 22$ , and the majority of them require  $\sim 1.5$  hr exposure time with an Echellette spectrograph on a 10 m class telescope to reach a sufficient S/N at  $R \sim 8000$  (e.g., see the Keck/ESI survey of DLAs by Rafelski et al. 2012).

To address the last challenge, we need a more efficient method to obtain SMG redshifts. One potential approach

is to exploit the frequency scan mode offered by modern millimeter interferometers. This method has the additional advantage of bypassing the interferometer imaging step because the primary beam is usually larger than the Herschel positional uncertainty and the line detection also provides positional information. For instance, with NOEMA scans of the 2 mm and 3 mm bands (only two spectral configurations per band), Neri et al. (2020) obtained 12 secure redshifts for 13 sources. The average telescope time spent is  $\sim 105$  minutes per source, including  $\sim 40$  minutes overhead. Although the targets in this pilot study have  $500\ \mu\text{m}$  flux densities greater than  $80\ \text{mJy}$  (many are strongly lensed), this technique could be applied to fainter sources (like ours with  $S_{500} > 20\ \text{mJy}$ ) as the instrument sensitivity and overheads continue to improve.

We thank D. Kereš and J. Hennawi for discussions. This work is partially supported by the National Science Foundation (NSF) grant AST-1614326. D.N. acknowledges support from NSF AST-1909153. The National Radio Astronomy Observatory is a facility of the NSF operated under cooperative agreement by Associated Universities, Inc. This paper makes use of the following ALMA data: ADS/JAO.ALMA#2015.1.00131.S, ADS/JAO.ALMA#2018.1.00548.S. ALMA is a partnership of ESO (representing its member states), NSF (USA) and NINS (Japan), together with NRC (Canada), MOST and ASIAA (Taiwan), and KASI (Republic of Korea), in cooperation with the Republic of Chile. The Joint ALMA Observatory is operated by ESO, AUI/NRAO, and NAOJ.

*Facilities:* Herschel, ALMA, Gemini/GNIRS, VLT/X-shooter, Keck/LRIS, Sloan, KiDS, VISTA.

## Appendix A Lensing of the SMG

In the KiDS *gri* pseudocolor image in Figure 1, there is an extended optical source just  $0''.8$  to the NW of the ALMA source. This offset cannot be an astrometric error, because the ALMA CO(3–2) emission of QSO2 agrees with its KiDS optical position within  $0''.1$ . The optical source is in the KiDS–VISTA nine-band photometric catalog (*ugriZYJHK<sub>s</sub>*; Kuijken et al. 2019) with a designation of KiDSDR4 J091339.496–010656.17 and a photometric redshift of  $z_p = 0.07_{-0.04}^{+0.05}$ . We obtained an optical spectrum with the Low Resolution Imaging Spectrometer (LRIS; Oke et al. 1995) on the Keck I telescope on 2017 March 23. Strong emission lines, such as [O II]  $\lambda 3728$ , [O III]  $\lambda \lambda 4960, 5008$ , were detected at high significance in the 20 minutes exposure, placing its redshift at 0.055.

The source is detected in all of the nine photometric bands included in the KiDS–VISTA photometric catalog, with  $r = 21.58 \pm 0.02$  and  $K_s = 20.84 \pm 0.18$ . Our best-fit stellar population synthesis model of the photometry reveals a stellar mass of  $\sim 3 \times 10^7 M_{\odot}$  and an SFR of  $\sim 0.006 M_{\odot} \text{ yr}^{-1}$ . We have used the models of Bruzual & Charlot (2003) assuming exponentially declining star-forming histories and the initial mass function of Chabrier (2003).

Could the SMG be gravitationally magnified by this foreground dwarf galaxy? Using the relation between halo mass and stellar mass from abundance matching (Figure 6 of Bullock & Boylan-Kolchin 2017), we estimate a halo mass of  $\sim 3 \times 10^{10} M_{\odot}$ . The halo mass corresponds to a line-of-sight velocity dispersion ( $\sigma$ ) of just  $\sim 29\ \text{km s}^{-1}$ , assuming a singular

isothermal sphere (SIS;  $\rho(r) = \sigma^2/2\pi Gr^2$ ) and the fitting function of the halo overdensity  $\Delta_c(z)$  from Bryan & Norman (1998). The Einstein radius of the SIS can be calculated as (e.g., Kneib & Natarajan 2011)

$$r_E = 4\pi \frac{\sigma^2}{c^2} \frac{D_{ds}}{D_s} \quad (\text{A1})$$

where  $c$  is the speed of light,  $D_{ds}$  is the angular diameter distance between the deflector and the background source, and  $D_s$  is the angular diameter distance between the observer and the background source. For our system consisting of a foreground lens at  $z_d = 0.055$  with  $\sigma = 29 \text{ km s}^{-1}$  and a background source at  $z_s = 2.674$ , the Einstein radius is  $r_E \sim 0''.024$ . Because  $r_E$  is  $33\times$  smaller than the  $0''.8$  offset between the SMG and the foreground galaxy, we conclude that the foreground galaxy is unlikely to have any measurable lensing effect on the SMG.

## Appendix B Blind Line Detection in the ALMA Band-3 Data

To search for faint emission-line sources with unknown line widths in 3D data cubes, a matched-filtering algorithm is commonly used: e.g., in SoFiA (Serra et al. 2015), FindClump (Walter et al. 2016), LineSeeker (González-López et al. 2019), and MF3D (Pavesi et al. 2018). We wrote an IDL program to implement this simple algorithm. The convolution kernel we chose to filter the data in the spectral dimension is a top-hat function with a variable half-width between  $n = 1$  and  $n = 9$ . For each channel, the data in the neighboring  $\pm n$  channels are stacked with equal weighting. Given the average channel spacing of  $\sim 25 \text{ km s}^{-1}$ , the convolved channel widths range between  $\sim 75 \text{ km s}^{-1}$  and  $\sim 475 \text{ km s}^{-1}$ . As shown in González-López et al. (2019), the simple top-hat function is as effective as the more sophisticated Gaussian kernels in detecting low-S/N line emission.

In each convolved channel map, we measure the rms noise level with a robust sigma routine and detect unresolved sources near the pixel with the highest S/N. An elliptical Gaussian fixed to the shape of the core of the dirty beam is fit to the  $8'' \times 8''$  subregion centered on the pixel and subtracted from the image. The parameters of the best-fit Gaussians are saved at each iteration to form the raw source catalog. The iterative process continues until the image contains no pixels above the S/N threshold of  $S/N_{\text{pix,th}} = 4.5$ . It is worth noting that this source-detection algorithm is similar to the minor cycles of the CLEAN deconvolution algorithm, but here we subtract only the core of the dirty beam to save computing time. This simplified approach is justified by the low S/N of the sources other than the SMG.

Given that a single source can be detected in multiple channels and with multiple convolution kernels, we remove duplicated detections by iteratively looping through the raw source list from the highest to the lowest S/N and discard all detections within  $2''$  and 0.2 GHz of the source with the highest S/N remaining in the list.

Because our search is restricted to point sources, the source S/N simply scales with the ratio between the peak of the best-fit Gaussian ( $S_{\text{peak}}$ ) and the rms noise of the convolved channel

map:

$$S/N = 0.77 \frac{S_{\text{peak}}}{\text{rms}}, \quad (\text{B1})$$

where a scaling factor is used to account for fitting errors (Equation (9) of Rengelink et al. 1997, see also Condon 1997).

To estimate the fidelity of the detected sources, we search for sources in simulated noise-only interferometer data instead of using negative “sources” in the actual data (e.g., González-López et al. 2019). First, we introduce random thermal noise by replacing the calibrated MS’s visibilities with a normally distributed random array of complex numbers generated with *numpy.random*. This is equivalent to the CASA simulator function `setnoise` in the “simplenoise” mode, but our approach is faster because it only writes the DATA column once and does not add MODEL\_DATA and CORRECTED\_DATA columns to the MS. Unlike the fixed random number seed (11111) adopted in the CASA simulator, each noise realization uses a different seed in our code. We set the widths of the normal distributions for the real and imaginary parts to the standard deviations of the original visibilities measured with `visstat` ( $\sigma \sim 250 \text{ mJy visibility}^{-1}$  with a slight dependence on the spectral window). Then, we use `tclean` to image the noise-only visibilities into spectral data cubes with natural weighting. The same `tclean` parameters are adopted except that we turn off deconvolution by setting `niter = 0`, because the simulated data contain no sources. For each spectral window, we generate a set of 10 simulated data cubes to provide enough source counts for the calculation of source fidelity.

We run the same line search code on the simulated data with the same detection parameters. We compare the normalized cumulative distribution functions (CDFs) of the detected sources in the actual data and in the simulated data to estimate the source fidelity. We use the following equation, similar to LineSeeker used in the ASPECS-LP survey

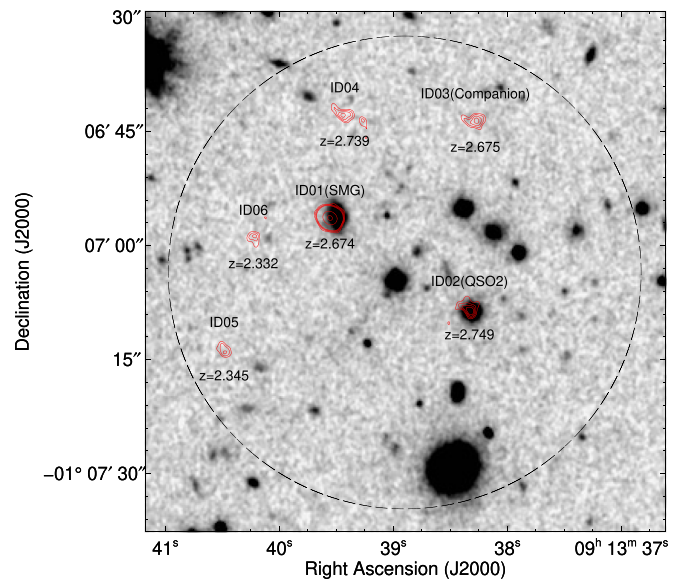


**Figure B1.** ALMA emission-line detections in the GAMA J0913–0107 field. The KiDS  $r$ -band image is overlaid with contours from the ALMA band-3 emission line sources. Each emission line source is labeled with its ID number and redshift (when interpreted as CO(3–2)). The long-dashed circle shows the ALMA primary beam at 94 GHz.

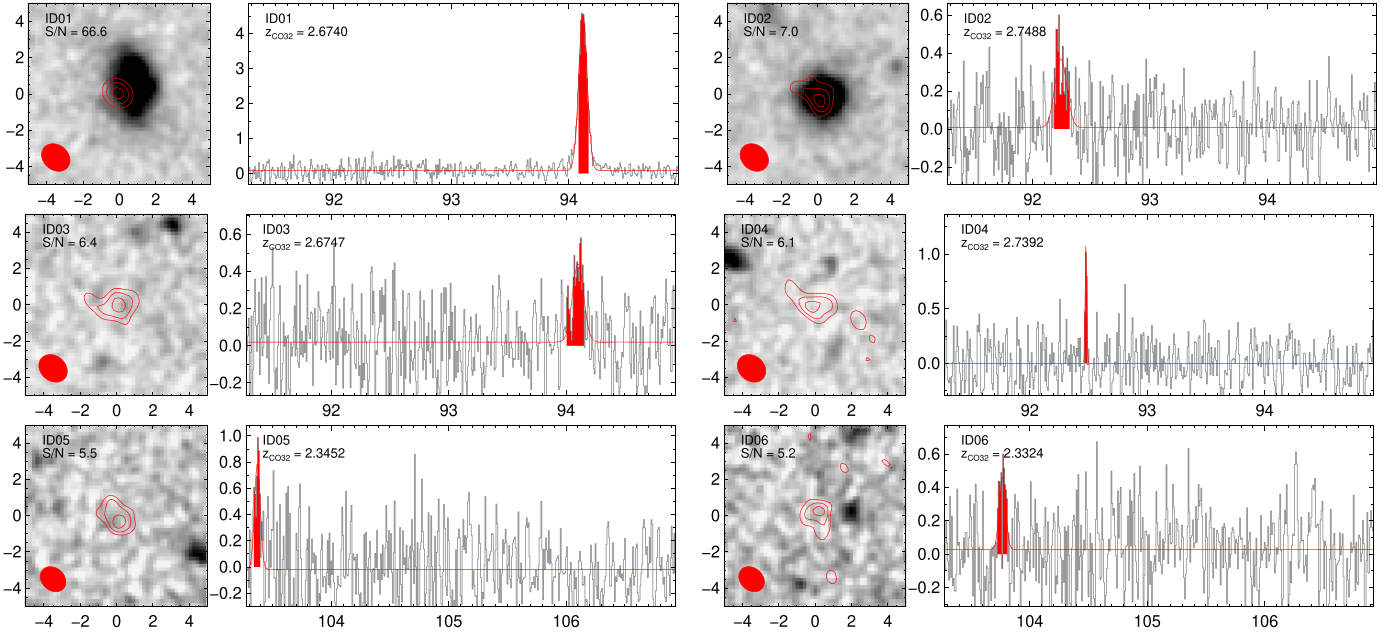


**Figure B2.** For each line emitter, we show a  $10'' \times 10''$  KiDS cutout image overlaid with its ALMA line emission map as contours, along with the integrated spectrum of the source (flux density in mJy vs. observed frequency in GHz). The ALMA maps are created by integrating line emission over narrow spectral windows, highlighted in red in their corresponding spectra. The red filled ellipses illustrate the synthesized beam size.

**Table B1**  
Line Emitters Found in the ALMA Band-3 Data (Sorted by S/N)

ID	R.A. (J2000) (h:m:s)	Decl. (J2000) (d:m:s)	$n$	S/N	Fidelity	$\nu_{\text{obs}}$ (GHz)	FWHM ( $\text{km s}^{-1}$ )	Line Flux ( $\text{Jy km s}^{-1}$ )	$z_{\text{CO3-2}}$	$L'_{\text{CO32}}$ ( $\text{K km s}^{-1} \text{pc}^2$ )	PB
1	09:13:39.55	-01:06:56.5	5	66.6	1.00	94.120	$271 \pm 5$	$1.3435 \pm 0.0264$	$2.6740 \pm 0.0001$	$10.69 \pm 0.01$	0.92
2	09:13:38.33	-01:07:08.4	8	7.0	1.00	92.241	$388 \pm 69$	$0.1482 \pm 0.0282$	$2.7488 \pm 0.0004$	$9.75 \pm 0.08$	0.95
3	09:13:38.28	-01:06:43.8	9	6.4	1.00	94.102	$358 \pm 67$	$0.1724 \pm 0.0318$	$2.6747 \pm 0.0003$	$9.80 \pm 0.08$	0.73
4	09:13:39.42	-01:06:43.0	1	6.1	1.00	92.479	$51 \pm 10$	$0.0590 \pm 0.0134$	$2.7392 \pm 0.0001$	$9.35 \pm 0.10$	0.74
5	09:13:40.47	-01:07:13.8	3	5.5	1.00	103.371	$166 \pm 32$	$0.1509 \pm 0.0293$	$2.3452 \pm 0.0002$	$9.64 \pm 0.08$	0.58
6	09:13:40.22	-01:06:59.1	5	5.2	0.97	103.767	$184 \pm 53$	$0.0488 \pm 0.0260$	$2.3324 \pm 0.0002$	$9.15 \pm 0.23$	0.72

**Note.** The column  $n$  lists the half-width of the convolution window that yielded the detection with the highest S/N. The columns Line Flux and  $L'_{\text{CO32}}$  have been corrected for the primary beam pattern, and the corresponding correction factors are listed in the column PB.

(González-López et al. 2019):

$$\text{Fidelity} = 1 - \frac{F_{\text{sim}}(\geq \text{S/N} | n)}{F_{\text{data}}(\geq \text{S/N} | n)}, \quad (\text{B2})$$

where  $F(\geq \text{S/N} | n)$  is the fraction of sources detected at or above the source S/N, with its detection kernel width  $n$ , and at any frequency channel in the spectral window. The subscript indicates whether it is from the actual data or the simulated noise-only data.  $F_{\text{data}}$  is measured directly from the CDF, while  $F_{\text{sim}}$  is obtained from the best-fit error function of the CDF to mitigate noise at high S/N due to low source counts. The fidelity is thus the probability that the detected source is not due to random noise. A source has a high fidelity near unity when  $F_{\text{sim}} \ll F_{\text{data}}$ , and a low fidelity near zero when  $F_{\text{sim}} \approx F_{\text{data}}$ .

We identified a total of six emission-line sources with fidelity  $> 0.9$  within the primary beam from the non-interpolated data cubes of all four spectral windows. We extracted the spectrum for each detection from the linear-interpolated and primary-beam-corrected data cubes with an elliptical aperture matched to the sizes of the restoring beams, i.e., we had assumed that the sources are unresolved. We measured the

central frequency ( $\nu_0$ ), FWHM, and line flux with a single-Gaussian model and list the results in Table B1. Figure B1 illustrates the distribution of the detected sources in the field, and Figure B2 shows the zoomed-in version of the integrated intensity maps and their ALMA spectra.

## Appendix C Other Absorbers in the QSO Spectra

Using the low-resolution ( $R \sim 2000$ ) Baryon Oscillation Spectroscopic Survey (BOSS) spectrum of QSO1, Noterdaeme et al. (2012b) identified two DLA candidates at  $z_{\text{abs}} = 2.680$  and 2.751. Subsequently, a number of Mg II and C IV absorbers were identified toward both QSOs using the BOSS spectra:  $z_{\text{abs}} = 0.9388, 2.2530, 2.7512$  toward QSO1 and  $z_{\text{abs}} = 0.7876, 1.0126, 1.5010, 2.7248, 2.7418$  toward QSO2 (Chen et al. 2015, 2016). The X-shooter spectra confirm all of the previously known absorbers and reveal several additional absorbers toward both QSOs:  $z_{\text{abs}} = 1.0855, 2.283, 2.9147$  toward QSO1 and  $z_{\text{abs}} = 0.886, 1.0865, 2.2525, 2.2845, 2.3065, 2.3445, 2.3595$  toward QSO2. Figure C1 shows portions of the X-shooter spectra to illustrate all of the major absorbers we have identified (8 toward QSO1 and 12 toward

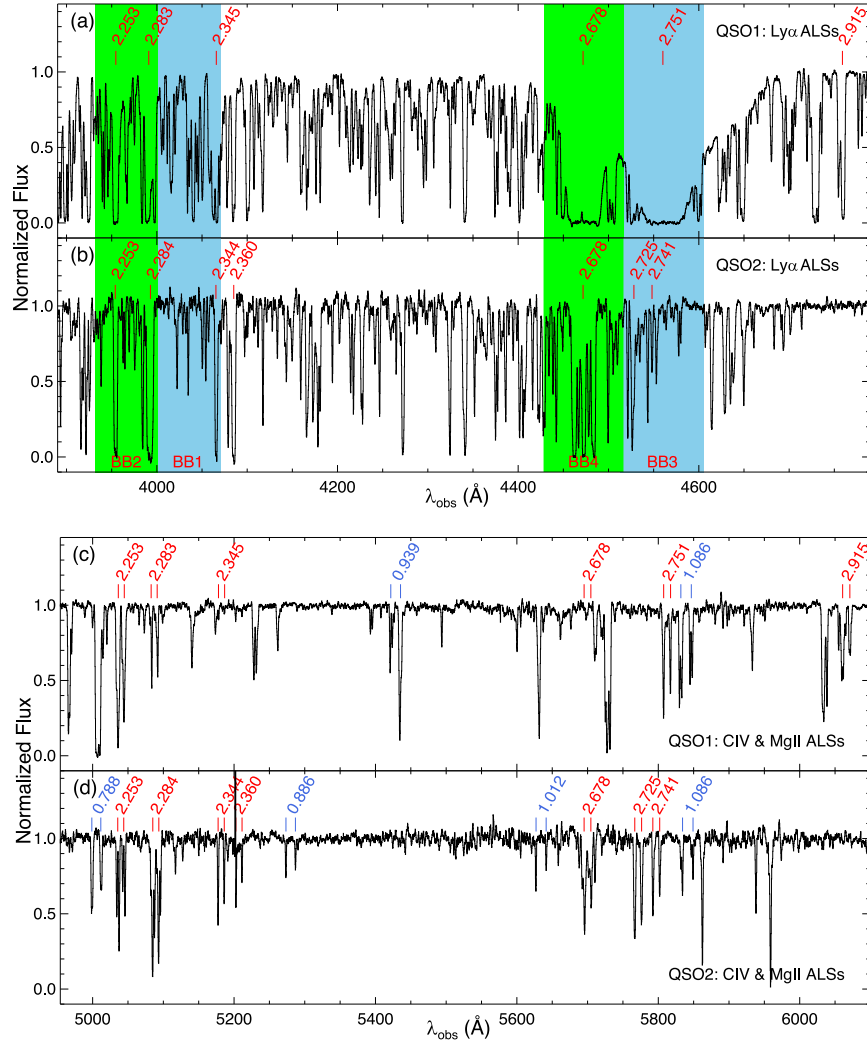


**Figure C1.** Continuum-normalized QSO spectra from X-shooter. (a), (b) Labeled are the main H I Ly $\alpha$  absorbers in the range  $2.20 < z_{\text{abs}} < 2.94$ . The redshift ranges covered by the ALMA observations for CO(3–2) are highlighted. (c), (d) Labeled in red are the main C IV  $\lambda\lambda 1548.2, 1550.8$  absorbers in the range  $2.20 < z_{\text{abs}} < 2.94$  and in blue the main Mg II  $\lambda\lambda 2796.4, 2803.5$  absorbers in the range  $0.77 < z_{\text{abs}} < 1.18$ .

**Table C1**  
Metal-line Measurements of the  $z_{\text{abs}} \approx 2.75$  DLA toward QSO1

Ion	$\lambda_{\text{rest}}$ ( $\text{\AA}$ )	EW ( $\text{\AA}$ )	$\log(N/\text{cm}^{-2})$	[X/H]'	[X/H]
C II	1334.5323	$2.13 \pm 0.01$	$> 15.48$	$> -2.25$	$> -2.26$
C IV	1548.2040	$0.63 \pm 0.02$	$14.40 \pm 0.03$	$-3.33 \pm 0.10$	$-1.31 \pm 0.10$
...	1550.7776	$0.45 \pm 0.02$	$14.50 \pm 0.04$	$-3.23 \pm 0.11$	$-1.21 \pm 0.11$
O I	1302.1685	$1.94 \pm 0.01$	$> 15.86$	$> -2.13$	$> -2.14$
Mg II	2796.3543	$4.37 \pm 0.04$	$> 14.44$	$> -2.46$	$> -2.26$
...	2803.5315	$3.40 \pm 0.08$	$> 14.59$	$> -2.31$	$> -2.11$
Al II	1670.7886	$1.88 \pm 0.01$	$> 13.99$	$> -1.76$	$> -1.52$
Al III	1854.7183	$0.43 \pm 0.01$	$13.45 \pm 0.05$	$-2.30 \pm 0.11$	$-1.59 \pm 0.11$
Si II	1260.4221	$2.07 \pm 0.00$	$> 14.54$	$> -2.27$	$> -2.31$
...	1304.3702	$1.69 \pm 0.01$	$> 15.46$	$> -1.35$	$> -1.40$
...	1526.7070	$1.89 \pm 0.02$	$> 15.23$	$> -1.58$	$> -1.63$
Si IV	1393.7602	$0.67 \pm 0.01$	$13.98 \pm 0.02$	$-2.83 \pm 0.10$	$-1.48 \pm 0.10$
...	1402.7729	$0.24 \pm 0.01$	$13.79 \pm 0.07$	$-3.02 \pm 0.12$	$-1.68 \pm 0.12$
Fe II	1608.4508	$1.33 \pm 0.01$	$15.22 \pm 0.01$	$-1.58 \pm 0.10$	$-1.62 \pm 0.10$
...	2382.7642	$3.01 \pm 0.03$	$> 14.67$	$> -2.13$	$> -2.16$
...	2600.1725	$3.16 \pm 0.03$	$> 14.73$	$> -2.07$	$> -2.10$

**Note.** All measurements were made using a velocity integration window between 0 and  $550 \text{ km s}^{-1}$  relative to  $z_{\text{sys}} = 2.7488$ . We use “<” for upper limits due to non-detections, “>” for lower limits due to line saturation, and “ $\lesssim$ ” for upper limits due to line blending.

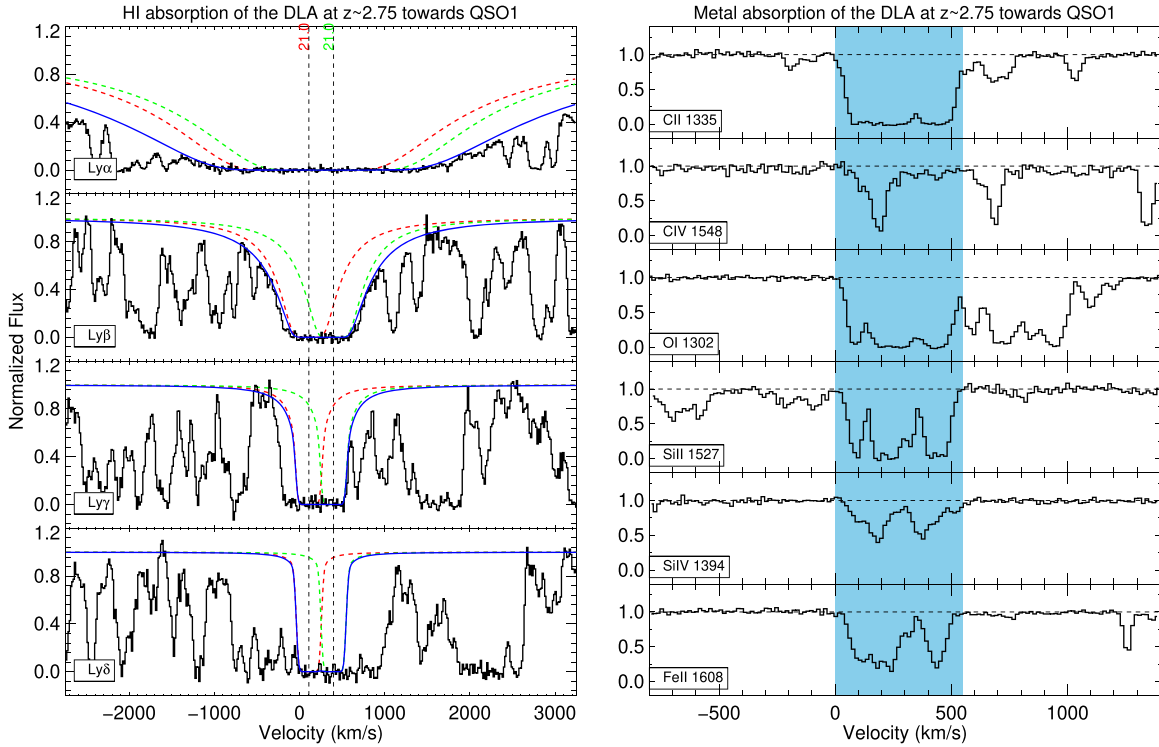


**Figure C2.** The DLA at  $z \approx 2.75$  toward QSO1. Left: H I Lyman series and Voigt profile fit (blue). Right: selected metal transitions and the adopted AODM velocity integration windows. All velocities are relative to the systemic redshift defined by the CO(3–2) line of QSO2 at  $z = 2.7488$ . The DLA is at an impact parameter of  $R_{\perp} = 85$  kpc.

QSO2), omitting only the Mg II absorber at  $z = 1.501$  toward QSO2.

The  $z_{\text{abs}} \approx 2.75$  DLA toward QSO1 is apparently associated with QSO2 at  $z = 2.7488$ . The DLA has been previously analyzed as part of the Quasar Probing Quasar (QPQ) project using a lower-resolution GMOS spectrum, from which they measured  $\log N_{\text{H I}} = 21.3 \pm 0.15$  (Prochaska et al. 2013a) and rest-frame equivalent widths of  $2.60 \pm 0.05 \text{ \AA}$  for C II  $\lambda 1334.5$  and  $0.51 \pm 0.05 \text{ \AA}$  for C IV  $\lambda 1548.2$  (Prochaska et al. 2014). We obtained similar results using the X-shooter spectrum (Figure C2). With Voigt profile fitting, we find that the H I Lyman series is adequately fit with two components separated by  $290 \text{ km s}^{-1}$  ( $z_{\text{abs}} = 2.7502, 2.7538$ ), each with  $\log N_{\text{H I}} = 21.0$  and  $b = 40 \text{ km s}^{-1}$ . We thus obtain a total column density of  $\log N_{\text{H I}} = 21.3$  with an estimated systematic uncertainty of  $\sim 0.1$  dex. With the AODM method and ICs from a CLOUDY model with  $\log N_{\text{H I}} = 21.3$ ,  $\log U = -2.5$ , and the HM12 radiation background, we measure an ionization-corrected  $\alpha$  metallicity of  $[\text{C}/\text{H}] = -1.2 \pm 0.1$  from C IV  $\lambda 1550.8$  and an iron metallicity of  $[\text{Fe}/\text{H}] = -1.6 \pm 0.2$  from Fe II  $\lambda 1608.5$  (see Table C1). Given the impact parameter of  $R_{\perp} = 85$  kpc, this DLA fits nicely with the CGM profiles of  $z = 2\text{--}3$  QSOs in Figure 8 (Lau et al. 2016).

## Appendix D The AODM Method and Results

This appendix gives a brief overview of the AODM method (Savage & Sembach 1991; Prochaska et al. 2001) and provides tables of ionic column densities, ionization corrections, and ionization-corrected metallicities for all of the selected metal transitions (Tables D1–D3). Equations are all in SI units. The

corresponding expressions in cgs units can be obtained by setting  $\epsilon_0 = 1/4\pi$ .

The velocity-dependent scattering cross section of resonance line photons is (Meiksin 2009)

$$\sigma(u) = \frac{\pi e^2}{m_e c} \left[ \frac{1}{4\pi \epsilon_0} \right] f \lambda_0 \phi_u, \quad (\text{D1})$$

where the constants  $e$ ,  $m_e$ ,  $\epsilon_0$ ,  $c$ ,  $f$ , and  $\lambda_0$  are respectively the electron charge, electron mass, the permeability of vacuum, the speed of light, the oscillator strength, and the rest-frame wavelength of the transition, and the function  $\phi_u$  is the probability density function per unit velocity due to line broadening (i.e., a Voigt profile). For QSO absorption lines, the optical depth ( $\tau(u)$ ) at velocity  $u$  is the product of this velocity-dependent cross section and the column density ( $N_a$ ):

$$\tau(u) = \frac{e^2}{4\epsilon_0 m_e c} f \lambda_0 N_a \phi_u \equiv \frac{e^2}{4\epsilon_0 m_e c} f \lambda_0 N_{a,u} \quad (\text{D2})$$

where we have defined the column density per unit velocity,  $N_{a,u} \equiv N_a \phi_u$ , by shifting the velocity dependence from the cross section to the column density.

The above relation provides a method to measure column densities from observed line profiles, because the optical depth is the natural logarithm of the ratio between the incident continuum intensity ( $I_0$ ) and the observed attenuated intensity ( $I_{\text{obs}}$ ):

$$\tau(u) = \ln \frac{I_0(u)}{I_{\text{obs}}(u)}. \quad (\text{D3})$$

The total column density can then be calculated by integrating the apparent optical depth over the velocity

**Table D1**  
AODM Ionic Column Densities

Ion	$\lambda_{\text{rest}}$ (Å)	$\log N$							
		QSO1-A1	QSO1-A2	QSO1-B1	QSO1-C1	QSO1-C2	QSO2-A2	QSO2-B1	QSO2-C1
C II	1334.5323	$\lesssim 14.74$	$13.94 \pm 0.05$	$< 12.90$	$> 15.21$	$14.18 \pm 0.03$	$14.01 \pm 0.06$	$< 13.33$	$< 13.25$
C IV	1548.2040	$< 12.88$	$< 12.88$	$< 12.91$	$14.08 \pm 0.04$	$< 12.91$	$< 13.20$	$14.23 \pm 0.03$	$13.61 \pm 0.08$
...	1550.7776	$< 13.21$	$< 13.19$	$< 13.19$	$14.15 \pm 0.07$	$\lesssim 14.83$	$\lesssim 14.30$	$14.30 \pm 0.04$	$13.72 \pm 0.13$
O I	1302.1685	$14.57 \pm 0.03$	$14.48 \pm 0.04$	$< 13.16$	$> 15.55$	$14.36 \pm 0.06$	$< 13.78$	$< 13.79$	$< 13.75$
Mg II	2796.3543	$13.24 \pm 0.07$	$12.99 \pm 0.08$	...	$> 14.09$	$13.21 \pm 0.05$	...	...	$< 12.60$
...	2803.5315	$13.49 \pm 0.06$	$13.15 \pm 0.09$	$\lesssim 14.11$	$> 14.32$	$13.08 \pm 0.09$	...	$< 12.93$	$< 12.76$
Al II	1670.7886	$12.37 \pm 0.11$	$11.97 \pm 0.28$	$< 11.70$	$13.49 \pm 0.02$	$12.15 \pm 0.20$	$12.28 \pm 0.19$	$< 12.12$	$< 12.06$
Al III	1854.7183	$< 12.17$	$< 12.14$	$< 12.15$	$12.91 \pm 0.16$	$< 12.12$	$< 12.50$	$< 12.53$	$< 12.49$
Si II	1304.3702	$13.76 \pm 0.12$	$13.22 \pm 0.40$	$< 12.93$	$14.81 \pm 0.02$	$13.32 \pm 0.34$	$< 13.52$	$< 13.55$	$< 13.48$
...	1526.7070	$13.78 \pm 0.08$	$< 13.23$	$< 13.15$	$14.76 \pm 0.02$	$13.55 \pm 0.12$	$< 13.58$	$< 13.50$	$< 13.38$
Si IV	1393.7602	$< 12.30$	$< 12.30$	$< 12.36$	$\lesssim 13.70$	$< 12.56$	$13.15 \pm 0.11$	$< 12.76$	$< 12.77$
...	1402.7729	$< 12.82$	$< 12.84$	$< 12.79$	$13.54 \pm 0.11$	$< 12.80$	$< 13.22$	$< 13.42$	$< 13.12$
Fe II	1608.4508	$13.55 \pm 0.26$	$< 13.39$	$< 13.44$	$14.52 \pm 0.05$	$< 13.36$	$< 13.64$	$< 13.74$	$< 13.71$
...	2382.7642	$13.34 \pm 0.05$	$12.90 \pm 0.13$	$< 12.58$	$\lesssim 14.47$	$\lesssim 13.90$	$< 12.79$	$< 12.66$	$< 12.71$
...	2600.1725	$\lesssim 13.64$	$13.13 \pm 0.10$	$< 12.58$	$> 14.25$	$12.91 \pm 0.17$	$< 13.18$	$< 12.92$	$< 12.94$

**Note.** This table lists the measured column densities from each transition, where we use “<” for upper limits due to non-detections, “>” for lower limits due to line saturation, “ $\lesssim$ ” for upper limits due to line blending, and “...” for no measurement due to poor data quality.

**Table D2**  
Ionization Correction

Ion	$IC \equiv \log f_{\text{H I}} - \log f_{\text{X}}$							
	QSO1-A1	QSO1-A2	QSO1-B1	QSO1-C1	QSO1-C2	QSO2-A2	QSO2-B1	QSO2-C1
C II	-0.18	-0.10	-1.74	-0.08	-0.58	-0.90	-1.74	-1.74
C IV	2.78	1.90	-2.82	2.00	1.98	0.40	-2.82	-2.82
O I	-0.01	-0.01	2.56	-0.01	-0.04	0.02	2.56	2.56
Mg II	0.14	0.25	0.04	0.27	-0.36	-0.71	0.04	0.04
Al II	-0.05	0.06	-1.08	0.12	-0.68	-1.20	-1.08	-1.08
Al II	0.61	0.55	-1.18	0.59	0.21	-0.51	-1.18	-1.18
Si II	-0.21	-0.14	-1.17	-0.12	-0.62	-0.95	-1.17	-1.17
Si IV	1.61	1.03	-2.37	1.13	0.83	-0.46	-2.37	-2.37
Fe II	-0.12	-0.08	1.58	-0.07	-0.37	-0.49	1.58	1.58

**Table D3**  
Ionization-corrected Metallicities

Ion	$\lambda_{\text{rest}}$ (Å)	$[X/H] \equiv [X/H]' + IC$							
		QSO1-A1	QSO1-A2	QSO1-B1	QSO1-C1	QSO1-C2	QSO2-A2	QSO2-B1	QSO2-C1
C II	1334.5323	$\lesssim -1.51$	$-2.66 \pm 0.08$	$< -1.25$	$> -1.53$	$-1.62 \pm 0.29$	$-1.91 \pm 0.34$	$< -0.87$	$< -0.92$
C IV	1548.2040	$< -0.41$	$< -1.72$	$< -2.32$	$-0.59 \pm 0.09$	$< -0.33$	$< -1.42$	$-1.05 \pm 0.19$	$-1.63 \pm 0.13$
...	1550.7776	$< -0.08$	$< -1.41$	$< -2.04$	$-0.52 \pm 0.10$	$\lesssim 1.59$	$\lesssim -0.32$	$-0.98 \pm 0.19$	$-1.53 \pm 0.16$
O I	1302.1685	$-1.77 \pm 0.06$	$-2.28 \pm 0.08$	$< 3.05$	$> -1.38$	$-1.15 \pm 0.30$	$< -1.48$	$< 3.63$	$< 3.62$
Mg II	2796.3543	$-1.87 \pm 0.09$	$-2.42 \pm 0.10$	...	$> -1.47$	$-1.53 \pm 0.29$	...	...	$< 1.04$
...	2803.5315	$-1.61 \pm 0.08$	$-2.26 \pm 0.11$	$\lesssim 2.57$	$> -1.24$	$-1.66 \pm 0.30$	...	$< 1.34$	$< 1.20$
Al II	1670.7886	$-1.77 \pm 0.12$	$-2.47 \pm 0.29$	$< 0.19$	$-1.08 \pm 0.08$	$-1.77 \pm 0.35$	$-1.96 \pm 0.38$	$< 0.56$	$< 0.52$
Al III	1854.7183	$< -1.31$	$< -1.82$	$< 0.54$	$-1.18 \pm 0.17$	$< -0.91$	$< -1.05$	$< 0.87$	$< 0.87$
Si II	1304.3702	$-1.60 \pm 0.13$	$-2.49 \pm 0.40$	$< 0.27$	$-1.05 \pm 0.08$	$-1.60 \pm 0.45$	$< -1.53$	$< 0.84$	$< 0.80$
...	1526.7070	$-1.57 \pm 0.09$	$< -2.48$	$< 0.48$	$-1.10 \pm 0.08$	$-1.37 \pm 0.31$	$< -1.48$	$< 0.79$	$< 0.70$
Si IV	1393.7602	$< -1.23$	$< -2.24$	$< -1.50$	$\lesssim -0.91$	$< -0.91$	$-1.41 \pm 0.35$	$< -1.14$	$< -1.11$
...	1402.7729	$< -0.72$	$< -1.70$	$< -1.07$	$-1.07 \pm 0.13$	$< -0.68$	$< -1.34$	$< -0.49$	$< -0.76$
Fe II	1608.4508	$-1.71 \pm 0.27$	$< -2.24$	$< 3.54$	$-1.27 \pm 0.09$	$< -1.30$	$< -0.94$	$< 3.79$	$< 3.79$
...	2382.7642	$-1.92 \pm 0.07$	$-2.73 \pm 0.15$	$< 2.68$	$\lesssim -1.33$	$\lesssim -0.76$	$< -1.79$	$< 2.71$	$< 2.80$
...	2600.1725	$\lesssim -1.62$	$-2.51 \pm 0.12$	$< 2.69$	$> -1.55$	$-1.76 \pm 0.34$	$< -1.39$	$< 2.98$	$< 3.02$

integration window:

$$N_a = \sum N_{a,u} \Delta u = \sum \frac{4\epsilon_0 m_e c}{e^2 f \lambda_0} \tau(u) \Delta u \quad (\text{D4})$$

and the  $1\sigma$  statistical variance on the column density through standard error propagation is

$$\sigma_{\text{sta}}^2(N_a) = \sum \left( \frac{4\epsilon_0 m_e c}{e^2 f \lambda_0} \right)^2 \sigma^2[\tau(u)] \Delta u^2 \quad (\text{D5})$$

where the statistical uncertainty of optical depth is estimated from the noise spectrum:

$$\sigma_{\text{sta}}[\tau(u)] = \sigma[I_{\text{obs}}(u)]/I_{\text{obs}}(u). \quad (\text{D6})$$

Similar to the HI Voigt profile fitting (but to a lesser extent because of the narrower velocity range), the ionic column density is also affected by the systematic uncertainty in our empirical model of the QSO continuum. We again adopt a  $\pm 10\%$  error in the QSO continuum ( $I_0$ ), which directly leads to  $\sigma_{\text{sys}}(\tau(u)) = 0.1$  and the equation for the systematic error of the ionic column density:

$$\sigma_{\text{sys}}^2(N_a) = \sum \left( \frac{4\epsilon_0 m_e c}{e^2 f \lambda_0} \right)^2 0.1^2 \Delta u^2. \quad (\text{D7})$$

## Appendix E

### The Identification of the Emission Counterpart of Subsystem C

In the deep  $r$ -band image from KiDS ( $5\sigma$  limit at  $\sim 25$  mag) shown in Figure E1(a), we labeled four faint optical sources within  $7''$  of QSO1. Here we explore whether any of these sources is connected to the DLA at  $z_{\text{abs}} \approx 2.68$  by examining their photometric redshifts and their ALMA spectra.

Three of the sources (A, B, C) are listed in the joint KiDS–VISTA nine-band photometric catalog (Kuijken et al. 2019):

1. KiDSDR4 J091338.791–010700.71 (A):  $r = 23.6 \pm 0.1$ ,  $H = 22.3 \pm 0.4$ ,  $z_p = 1.09_{-0.15}^{+0.09}$ ;
2. KiDSDR4 J091338.711–010705.48 (B):  $r = 24.5 \pm 0.2$ ,  $H = 22.9 \pm 0.7$ ,  $z_p = 0.45_{-0.12}^{+0.78}$ ;
3. KiDSDR4 J091338.527–010703.60 (C):  $r = 23.8 \pm 0.1$ ,  $H = 22.0 \pm 0.3$ ,  $z_p = 0.79_{-0.06}^{+0.45}$ .

where the  $r$ - and  $H$ -band magnitudes are from the homogenized ‘‘Gaussian aperture and PSF’’ photometry and  $z_p$  are the estimates of nine-band photometric redshift from the Bayesian photometric redshift code BPZ (Benítez 2000). The 68% confidence intervals of the photometric redshifts suggest that both sources are in the far foreground of the SMG SMM J0913 ( $z_{\text{SMG}} = 2.674$ ). The fourth object (D) is not in the catalog, likely because its proximity to the bright QSO1. We measured its position directly from the image: R.A. =  $09^{\text{h}}13^{\text{m}}39^{\text{s}}.05$ , decl. =  $-01^{\circ}07'06''.5$ .

We then extracted spectra at their optical positions from the ALMA band-3 data cube. For objects A, B, and D, we adopted elliptical apertures matching the synthesized beam size ( $1''.7 \times 1''.3$  at  $\text{PA} = 49^\circ$ ). We show these spectra in Figure E1(c). Even at the depth of our ALMA data ( $\text{rms} = 0.155 \text{ mJy beam}^{-1} \text{ channel}^{-1}$  in BB4), none of the sources show emission lines at a detectable level.

For Object C, we initially used an aperture centered on the optical position and detected hints of emission lines at the expected frequencies of absorption-line clouds C1 and C2. We then made a CO map by combining the two channels that show the most significant emission. The CO image in Figure E1(b) led to the discovery of Comp b because it reveals a highly significant source  $\sim 3''$  to the SSW of the optical position, which we have designated as Comp b. Guided by the CO image, we re-extracted a spectrum from a  $3''.4 \times 1''.8$  elliptical aperture that matches the geometry of Comp b to optimize the line detection. This spectrum is shown in the Object C panel of Figure E1(c). Line emission is clearly detected at the expected frequencies of absorption-line clouds C1 and C2 toward QSO1.

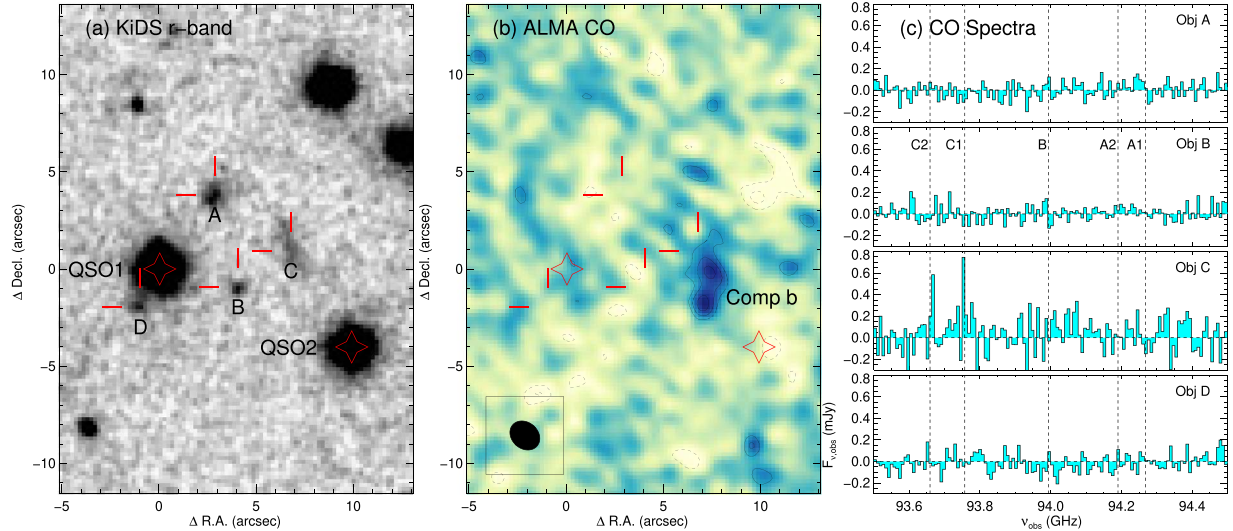


**Figure E1.** (a) The four faint ( $r > 23$ ) optical sources within  $7''$  of QSO1. (b) An ALMA CO map constructed by combining the channels at 93.7535 and 93.6676 GHz, where CO emission from Object C is detected. The contours are drawn at  $-3$ ,  $-2$  (dashed),  $2$ ,  $3$ , and  $4\sigma$  (solid). In both images, QSO1 sets the origin of the coordinates. (c) The four panels show the ALMA spectra of the objects. The vertical dashed lines indicate the CO(3–2) frequencies that correspond to the redshifts of the major absorption-line clouds toward QSO1.

Through this exercise, we have identified Comp b as the most likely emission counterpart of absorption subsystem C toward both QSOs.

### ORCID iDs

Hai Fu  <https://orcid.org/0000-0001-9608-6395>  
 R. Xue  <https://orcid.org/0000-0001-7689-9305>  
 J. X. Prochaska  <https://orcid.org/0000-0002-7738-6875>  
 M. W. Lau  <https://orcid.org/0000-0001-9755-9406>  
 D. Narayanan  <https://orcid.org/0000-0002-7064-4309>

### References

- Alaghband-Zadeh, S., Chapman, S. C., Swinbank, A. M., et al. 2012, *MNRAS*, **424**, 2232
- Asplund, M., Grevesse, N., Sauval, A. J., & Scott, P. 2009, *ARA&A*, **47**, 481
- Barger, A. J., Cowie, L. L., Sanders, D. B., et al. 1998, *Natur*, **394**, 248
- Benítez, N. 2000, *ApJ*, **536**, 571
- Birnboim, Y., & Dekel, A. 2003, *MNRAS*, **345**, 349
- Blain, A. W., Smail, I., Ivison, R. J., Kneib, J.-P., & Frayer, D. T. 2002, *PhR*, **369**, 111
- Bolatto, A. D., Wolfire, M., & Leroy, A. K. 2013, *ARA&A*, **51**, 207
- Bonato, M., Liuzzo, E., Herranz, D., et al. 2019, *MNRAS*, **485**, 1188
- Bothwell, M. S., Smail, I., Chapman, S. C., et al. 2013, *MNRAS*, **429**, 3047
- Bruzual, G., & Charlot, S. 2003, *MNRAS*, **344**, 1000
- Bryan, G. L., & Norman, M. L. 1998, *ApJ*, **495**, 80
- Bullock, J. S., & Boylan-Kolchin, M. 2017, *ARA&A*, **55**, 343
- Bullock, J. S., Kolatt, T. S., Sigad, Y., et al. 2001, *MNRAS*, **321**, 559
- Burbidge, E. M., Lynds, C. R., & Stockton, A. N. 1968, *ApJ*, **152**, 1077
- Cantalupo, S., Arrigoni-Battaia, F., Prochaska, J. X., Hennawi, J. F., & Madau, P. 2014, *Natur*, **506**, 63
- Casey, C. M., Narayanan, D., & Cooray, A. 2014, *PhR*, **541**, 45
- Chabrier, G. 2003, *PASP*, **115**, 763
- Chapman, S. C., Blain, A. W., Smail, I., & Ivison, R. J. 2005, *ApJ*, **622**, 772
- Chen, C.-C., Smail, I., Swinbank, A. M., et al. 2015, *ApJ*, **799**, 194
- Chen, Y.-M., Shi, Y., Tremonti, C. A., et al. 2016, *NatCo*, **7**, 13269
- Condon, J. J. 1997, *PASP*, **109**, 166
- Crighton, N. H. M., Hennawi, J. F., & Prochaska, J. X. 2013, *ApJL*, **776**, L18
- Crighton, N. H. M., Hennawi, J. F., Simcoe, R. A., et al. 2015, *MNRAS*, **446**, 18
- Cushing, M. C., Vacca, W. D., & Rayner, J. T. 2004, *PASP*, **116**, 362
- Daddi, E., Dannerbauer, H., Stern, D., et al. 2009, *ApJ*, **694**, 1517
- Daddi, E., Elbaz, D., Walter, F., et al. 2010, *ApJL*, **714**, L118
- Daddi, E., Valentino, F., Rich, R. M., et al. 2020, arXiv:2006.11089
- Decarli, R., Walter, F., González-López, J., et al. 2019, *ApJ*, **882**, 138
- Dekel, A., & Birnboim, Y. 2006, *MNRAS*, **368**, 2
- Dekel, A., Birnboim, Y., Engel, G., et al. 2009, *Natur*, **457**, 451
- Downes, D., & Solomon, P. M. 1998, *ApJ*, **507**, 615
- Dunne, L., Eales, S., Edmunds, M., et al. 2000, *MNRAS*, **315**, 115
- Eales, S. A., Raymond, G., Roseboom, I. G., et al. 2010, *A&A*, **518**, L23
- Eastman, J., Gaudi, B. S., & Agol, E. 2013, *PASP*, **125**, 83
- Eastman, J. D., Rodríguez, J. E., Agol, E., et al. 2019, arXiv:1907.09480
- Elias, J. H., Joyce, R. R., Liang, M., et al. 2006, *Proc. SPIE*, **6269**, 62694C
- Erb, D. K., Shapley, A. E., Pettini, M., et al. 2006, *ApJ*, **644**, 813
- Falgarone, E., Zwaan, M. A., Godard, B., et al. 2017, *Natur*, **548**, 430
- Faucher-Giguère, C.-A., Feldmann, R., Quataert, E., et al. 2016, *MNRAS*, **461**, L32
- Faucher-Giguère, C.-A., Hopkins, P. F., Kereš, D., et al. 2015, *MNRAS*, **449**, 987
- Ferland, G. J., Chatzikos, M., Guzmán, F., et al. 2017, *RMxAA*, **53**, 385
- Field, G. B., & Steigman, G. 1971, *ApJ*, **166**, 59
- Finley, H., Petitjean, P., Noterdaeme, P., & Pâris, I. 2014, *A&A*, **572**, A31
- Fu, H., Cooray, A., Feruglio, C., et al. 2013, *Natur*, **498**, 338
- Fu, H., Hennawi, J. F., Prochaska, J. X., et al. 2016, *ApJ*, **832**, 52
- Fu, H., Isbell, J., Casey, C. M., et al. 2017, *ApJ*, **844**, 123
- Fumagalli, M., O'Meara, J. M., & Prochaska, J. X. 2016, *MNRAS*, **455**, 4100
- Fumagalli, M., Prochaska, J. X., Kasen, D., et al. 2011, *MNRAS*, **418**, 1796
- Fynbo, J. P. U., Geier, S. J., Christensen, L., et al. 2013, *MNRAS*, **436**, 361
- Fynbo, J. P. U., Heintz, K. E., Neeleman, M., et al. 2018, *MNRAS*, **479**, 2126
- Fynbo, J. P. U., Prochaska, J. X., Sommer-Larsen, J., Dessauges-Zavadsky, M., & Møller, P. 2008, *ApJ*, **683**, 321
- Genzel, R., Tacconi, L. J., Gracia-Carpio, J., et al. 2010, *MNRAS*, **407**, 2091
- González-López, J., Decarli, R., Pavesi, R., et al. 2019, *ApJ*, **882**, 139
- Greve, T. R., Bertoldi, F., Smail, I., et al. 2005, *MNRAS*, **359**, 1165
- Griffin, M. J., Abergel, A., Abreu, A., et al. 2010, *A&A*, **518**, L3
- Groves, B. A., Dopita, M. A., & Sutherland, R. S. 2004, *ApJS*, **153**, 9
- Haardt, F., & Madau, P. 2012, *ApJ*, **746**, 125
- Hainline, L. J., Blain, A. W., Smail, I., et al. 2011, *ApJ*, **740**, 96
- Harris, A. I., Baker, A. J., Zonak, S. G., et al. 2010, *ApJ*, **723**, 1139
- Hennawi, J. F., Prochaska, J. X., Burles, S., et al. 2006, *ApJ*, **651**, 61
- Hennawi, J. F., Prochaska, J. X., Cantalupo, S., & Arrigoni-Battaia, F. 2015, *Sci*, **348**, 779
- Hickox, R. C., Wardlow, J. L., Smail, I., et al. 2012, *MNRAS*, **421**, 284
- Hodge, J. A., Carilli, C. L., Walter, F., et al. 2012, *ApJ*, **760**, 11
- Ivison, R. J., Papadopoulos, P. P., Smail, I., et al. 2011, *MNRAS*, **412**, 1913
- James, A., Dunne, L., Eales, S., & Edmunds, M. G. 2002, *MNRAS*, **335**, 753
- Jorgenson, R. A., & Wolfe, A. M. 2014, *ApJ*, **785**, 16
- Juneau, S., Narayanan, D. T., Moustakas, J., et al. 2009, *ApJ*, **707**, 1217
- Kanekar, N., Prochaska, J. X., Neeleman, M., et al. 2020, *ApJL*, **901**, L5
- Kennicutt, R. C., Jr 1998, *ApJ*, **498**, 541
- Kennicutt, R. C., Jr, Bresolin, F., & Garnett, D. R. 2003, *ApJ*, **591**, 801
- Keres, D., Katz, N., Weinberg, D. H., & Davé, R. 2005, *MNRAS*, **363**, 2
- Kereš, D., Katz, N., Fardal, M., Davé, R., & Weinberg, D. H. 2009, *MNRAS*, **395**, 160
- Klypin, A. A., Trujillo-Gomez, S., & Primack, J. 2011, *ApJ*, **740**, 102
- Kneib, J.-P., & Natarajan, P. 2011, *A&ARv*, **19**, 47
- Krogager, J.-K., Møller, P., Fynbo, J. P. U., & Noterdaeme, P. 2017, *MNRAS*, **469**, 2959
- Kuijken, K., Heymans, C., Dvornik, A., et al. 2019, *A&A*, **625**, A2
- Lau, M. W., Prochaska, J. X., & Hennawi, J. F. 2016, *ApJS*, **226**, 25
- Lehner, N., O'Meara, J. M., Howk, J. C., Prochaska, J. X., & Fumagalli, M. 2016, *ApJ*, **833**, 283
- Li, Q., Cai, Z., Prochaska, J. X., et al. 2019, *ApJ*, **875**, 130
- Lovell, C. C., Geach, J. E., Davé, R., Narayanan, D., & Li, Q. 2021, *MNRAS*, **502**, 772
- Magnelli, B., Lutz, D., Santini, P., et al. 2012b, *A&A*, **539**, 155
- Magnelli, B., Saintonge, A., Lutz, D., et al. 2012a, *A&A*, **548**, 22
- Martin, C. L., Ho, S. H., Kacprzak, G. G., & Churchill, C. W. 2019, *NatAs*, **3**, 822
- Martin, D. C., Matuszewski, M., Morrissey, P., et al. 2015, *Natur*, **524**, 192
- Meiksin, A. A. 2009, *RvMP*, **81**, 1405
- Michałowski, M. J., Dunlop, J. S., Cirasuolo, M., et al. 2012, *A&A*, **541**, 85
- Møller, P., & Christensen, L. 2020, *MNRAS*, **492**, 4805
- Møller, P., Fynbo, J. P. U., Ledoux, C., & Nilsson, K. K. 2013, *MNRAS*, **430**, 2680
- Møller, P., & Fynbo, J. U. 2001, *A&A*, **372**, L57
- Morton, D. C. 2003, *ApJS*, **149**, 205
- Narayanan, D., Turk, M., Feldmann, R., et al. 2015, *Natur*, **525**, 496
- Navarro, J. F., Frenk, C. S., & White, S. D. M. 1996, *ApJ*, **462**, 563
- Neeleman, M., Kanekar, N., Prochaska, J. X., et al. 2017, *Sci*, **355**, 1285
- Neeleman, M., Kanekar, N., Prochaska, J. X., Rafelski, M. A., & Carilli, C. L. 2019, *ApJL*, **870**, L19
- Neeleman, M., Wolfe, A. M., Prochaska, J. X., & Rafelski, M. 2013, *ApJ*, **769**, 54
- Neri, R., Cox, P., Omont, A., et al. 2020, *A&A*, **635**, A7
- Noterdaeme, P., Laursen, P., Petitjean, P., et al. 2012a, *A&A*, **540**, A63
- Noterdaeme, P., Petitjean, P., Carithers, W. C., et al. 2012b, *A&A*, **547**, L1
- Oke, J. B., Cohen, J. G., Carr, M., et al. 1995, *PASP*, **107**, 375
- Oser, L., Ostriker, J. P., Naab, T., Johansson, P. H., & Burkert, A. 2010, *ApJ*, **725**, 2312
- Papadopoulos, P. P., van der Werf, P., Xilouris, E., Isaak, K. G., & Gao, Y. 2012, *ApJ*, **751**, 10
- Pâris, I., Petitjean, P., Aubourg, É., et al. 2012, *A&A*, **548**, A66
- Pascale, E., Auld, R., Dariush, A., et al. 2011, *MNRAS*, **415**, 911
- Pavesi, R., Sharon, C. E., Riechers, D. A., et al. 2018, *ApJ*, **864**, 49
- Péroux, C., & Howk, J. C. 2020, *ARA&A*, **58**, 363
- Planck Collaboration, Aghanim, N., Akrami, Y., et al. 2020, *A&A*, **641**, A6
- Press, W. H., Teukolsky, S. A., Vetterling, W. T., & Flannery, B. P. 1992, *Numerical Recipes in C. The Art of Scientific Computing* (2nd ed.; Cambridge: Cambridge Univ. Press)
- Prochaska, J. X. 1999, *ApJL*, **511**, L71
- Prochaska, J. X., Hennawi, J. F., Lee, K.-G., et al. 2013a, *ApJ*, **776**, 136
- Prochaska, J. X., Hennawi, J. F., & Simcoe, R. A. 2013b, *ApJL*, **762**, L19
- Prochaska, J. X., Lau, M. W., & Hennawi, J. F. 2014, *ApJ*, **796**, 140
- Prochaska, J. X., Neeleman, M., Kanekar, N., & Rafelski, M. 2019, *ApJL*, **886**, L35
- Prochaska, J. X., Wolfe, A. M., Tytler, D., et al. 2001, *ApJS*, **137**, 21
- Rafelski, M., Wolfe, A. M., Prochaska, J. X., Neeleman, M., & Mendez, A. J. 2012, *ApJ*, **755**, 89

- Rauch, M. 1998, *ARA&A*, 36, 267
- Rengelink, R. B., Tang, Y., de Bruyn, A. G., et al. 1997, *A&AS*, 124, 259
- Riechers, D. A., Hodge, J., Walter, F., Carilli, C. L., & Bertoldi, F. 2011, *ApJL*, 739, L31
- Rigby, E. E., Maddox, S. J., Dunne, L., et al. 2011, *MNRAS*, 415, 2336
- Rubin, K. H. R., Hennawi, J. F., Prochaska, J. X., et al. 2015, *ApJ*, 808, 38
- Rudie, G. C., Steidel, C. C., Shapley, A. E., & Pettini, M. 2013, *ApJ*, 769, 146
- Rudie, G. C., Steidel, C. C., Trainor, R. F., et al. 2012, *ApJ*, 750, 67
- Saintonge, A., Lutz, D., Genzel, R., et al. 2013, *ApJ*, 778, 2
- Savage, B. D., & Sembach, K. R. 1991, *ApJ*, 379, 245
- Savage, B. D., & Sembach, K. R. 1996, *ApJ*, 470, 893
- Serra, P., Westmeier, T., Giese, N., et al. 2015, *MNRAS*, 448, 1922
- Sharon, C. E., Baker, A. J., Harris, A. I., & Thomson, A. P. 2013, *ApJ*, 765, 6
- Simcoe, R. A., Sargent, W. L. W., & Rauch, M. 2004, *ApJ*, 606, 92
- Simcoe, R. A., Sargent, W. L. W., Rauch, M., & Becker, G. 2006, *ApJ*, 637, 648
- Smail, I., Ivison, R. J., & Blain, A. W. 1997, *ApJL*, 490, L5
- Srianand, R., Hussain, T., Noterdaeme, P., et al. 2016, *MNRAS*, 460, 634
- Steidel, C. C., & Hamilton, D. 1992, *AJ*, 104, 941
- Swinbank, A. M., Smail, I., Chapman, S. C., et al. 2004, *ApJ*, 617, 64
- Tacconi, L. J., Genzel, R., Saintonge, A., et al. 2018, *ApJ*, 853, 179
- Tacconi, L. J., Genzel, R., Smail, I., et al. 2008, *ApJ*, 680, 246
- Tacconi, L. J., Neri, R., Genzel, R., et al. 2013, *ApJ*, 768, 74
- Targett, T. A., Dunlop, J. S., Cirasuolo, M., et al. 2013, *MNRAS*, 432, 2012
- Ter Braak, C. J. F. 2006, *Stat. Comput.*, 16, 239
- Theuns, T. 2021, *MNRAS*, 500, 2741
- Tremonti, C. A., Heckman, T. M., Kauffmann, G., et al. 2004, *ApJ*, 613, 898
- Umehata, H., Fumagalli, M., Smail, I., et al. 2019, *Sci*, 366, 97
- Valiante, E., Smith, M. W. L., Eales, S., et al. 2016, *MNRAS*, 462, 3146
- Vernet, J., Dekker, H., D'Odorico, S., et al. 2011, *A&A*, 536, A105
- Walter, F., Decarli, R., Aravena, M., et al. 2016, *ApJ*, 833, 67
- Wardlow, J. L., Smail, I., Coppin, K. E. K., et al. 2011, *MNRAS*, 415, 1479
- Weidinger, M., Møller, P., & Fynbo, J. P. U. 2004, *Natur*, 430, 999
- Wolfe, A. M., Gawiser, E., & Prochaska, J. X. 2005, *ARA&A*, 43, 861
- Wolfe, A. M., Turnshek, D. A., Smith, H. E., & Cohen, R. D. 1986, *ApJS*, 61, 249
- Xue, R., Fu, H., Isbell, J., et al. 2018, *ApJL*, 864, L11